The Signatures of Large-scale Temperature and Intensity Fluctuations in the Lyman-α Forest

Matthew McQuinn[1]*, Lars Hernquist[2], Adam Lidz[3], Matias Zaldarriaga[4]

[1] *Department of Astronomy, University of California, Berkeley, CA 94720, USA*
[2] *Harvard-Smithsonian Center for Astrophysics, 60 Garden St., Cambridge, MA 02138, USA*
[3] *Department of Physics and Astronomy, University of Pennsylvania; Philadelphia, PA 19104, USA*
[4] *Institute for Advanced Study, 1 Einstein Drive, Princeton, NJ 08540, USA*

14 July 2011

ABSTRACT

It appears inevitable that reionization processes would have produced large-scale temperature fluctuations in the intergalactic medium. Using toy temperature models and detailed heating histories from cosmological simulations of He II reionization, we study the consequences of inhomogeneous heating for the Lyα forest. The impact of temperature fluctuations in physically well-motivated models can be surprisingly subtle. In fact, we show that temperature fluctuations at the level predicted by our reionization simulations do not give rise to detectable signatures in the types of statistics that have been employed previously. However, because of the aliasing of small-scale density power to larger scale modes in the line-of-sight Lyα forest power spectrum, earlier analyses were not sensitive to 3D modes with $\gtrsim 30$ comoving Mpc wavelengths – scales where temperature fluctuations are likely to be relatively largest. The ongoing Baryon Oscillation Spectroscopic Survey (BOSS) aims to measure the 3D power spectrum of the Lyα forest, P_F, from a large sample of quasars in order to avoid this aliasing. We find that physically motivated temperature models can alter P_F at an order unity level at $k \lesssim 0.1$ comoving Mpc^{-1}, a magnitude that should be easily detectable with BOSS. Fluctuations in the intensity of the ultraviolet background can also alter P_F significantly. These signatures will make it possible for BOSS to study the thermal impact of He II reionization at $2 < z < 3$ and to constrain models for the sources of the ionizing background. Future spectroscopic surveys could extend this measurement to even higher redshifts, potentially detecting the thermal imprint of hydrogen reionization.

Key words: cosmology: theory – cosmology: large-scale structure – quasars: absorption lines – intergalactic medium

1 INTRODUCTION

The temperature of the intergalactic medium (IGM) is largely determined by how and when the cosmic hydrogen and helium were reionized. Measurements of the mean temperature of the IGM at redshifts $2 < z < 6$ appear to be consistent with the paradigm that hydrogen was reionized at $z \sim 10$ and helium was doubly ionized at $z \sim 3$ (Ricotti et al. 2000; Schaye et al. 2000; Zaldarriaga et al. 2001; McDonald et al. 2001; Hui & Haiman 2003; Lidz et al. 2010; Bolton et al. 2010; Becker et al. 2011). However, not all of these studies agree on the trends nor on their interpretation.

In addition to raising the mean temperature of the IGM, reionization processes would have heated the intergalactic gas inhomogeneously. Once imprinted, an intergalactic temperature fluctuation would fade away over roughly a Hubble time (Hui & Haiman 2003). Inhomogeneities in the temperature of the IGM alter the Lyα forest absorption because the ionization state of hydrogen depends on the temperature, because the gas distribution on $\lesssim 100$ kpc scales is smoothed by thermal pressure, and because of thermal broadening of the absorption features. However, the vast majority of studies of the Lyα forest have assumed that there is

* mmcquinn@berkeley.edu

an approximately power-law relationship between temperature and density. Our study investigates the detectability of realistic models for temperature inhomogeneities.

The level of intergalactic temperature fluctuations has been constrained by previous analyses of the forest. Theuns et al. (2002) and Lidz et al. (2010) placed upper limits on the allowed level of these fluctuations in the context of toy inhomogeneous heating models. In addition, the standard model for the Lyα forest has been successful at explaining the statistical properties of this absorption (Miralda-Escudé et al. 1996; Hernquist et al. 1996; Katz et al. 1996; Davé et al. 1999; McDonald et al. 2005). This picture posits that the fluctuations in the $2 \lesssim z \lesssim 5$ forest were driven primarily by density inhomogeneities, that the gas temperature can be approximated as a power law in density, and that the photoionization rate was nearly spatially invariant. The success of this model implies that deviations from it cannot be large.

Several theoretical studies of the Lyα forest have examined the impact of temperature inhomogeneities on various statistics. Lai et al. (2006) investigated the effect of temperature fluctuations on the Lyα forest line-of-sight power spectrum. Surprisingly, they found that models with $\mathcal{O}(1)$ fluctuations in the temperature ($\Delta T/T \sim 1$) that correlated over tens of comoving Mpc altered this statistic at *only* the few percent-level for $k < 5$ comoving Mpc^{-1} compared to models with power-law temperature-density relations.

Other statistics have been found to be more sensitive to such inhomogeneities. Meiksin (2000), Theuns & Zaroubi (2000), and Zaldarriaga (2002) advocated the use of wavelets filters as a means to spatially identify temperature inhomogeneities, and they showed that wavelets are sensitive to 10s of comoving Mpc fluctuations with $\Delta T/T \approx 1$ when applied to ≈ 10 high-resolution Lyα forest spectra. Lee & Spergel (2010) found that threshold clustering functions (a popular statistic in the material sciences) could discriminate between different allowed thermal states. Fang & White (2004) argued that a three-point statistic which correlates the large-scale flux with the small-scale power could place a strong constraint on deviations from a power-law temperature-density relation. Lastly, White et al. (2010) showed that large temperature fluctuations could have a significant effect on two- and three-point functions estimated from correlating multiple Lyα forest sightlines.

Here, we quantify the impact of 10s of comoving Mpc temperature fluctuations on a diverse set of Lyα forest statistics. We use both toy models as well as the He II reionization simulations presented in McQuinn et al. (2009) to understand these effects. Section 2 discusses the different nonstandard contributions to fluctuations in the forest, concentrating on inhomogeneities in the temperature. Section 3 describes the methods of analysis used in our study. Section 4 (and Appendix A) quantifies the impact of models for temperature inhomogeneities on different Lyα forest statistics. Section 5 discusses how fluctuations in the ionizing background could also alter Lyα forest statistics.

We adopt a flat ΛCDM cosmological model consistent with the most recent cosmological constraints (Komatsu et al. 2011), and we henceforth will use "Mpc" as shorthand for "comoving Mpc." All of our Lyα forest calculations normalize to the mean flux, $\langle F \rangle$, values of

Faucher-Giguère et al. (2008), which measured $\langle F \rangle = 0.69$ at $z = 3$ and $\langle F \rangle = 0.39$ at $z = 4$.

2 BACKGROUND

In the Sobolev approximation, the optical depth for a photon to be absorbed as it redshifts across the Lyα resonance of hydrogen is

$$\tau_{\mathrm{Ly}\alpha} \approx 1.1 \, \Delta_b^2 \, T_4^{-0.7} \, \Gamma_{-12}^{-1} \, \left(\frac{1+z}{4} \right)^{9/2} \, \frac{H(z)/(1+z)}{dv/dx}, \quad (1)$$

where Δ_b is the gas density in units of the cosmic mean, T_4 is the temperature in units of 10^4 K, $H(z)$ is the Hubble parameter, and dv/dx is the line-of-sight velocity gradient (which is equal to $H(z)/(1+z)$ in the absence of peculiar velocities). Equation (1) assumes that the hydrogen is in photoionization equilibrium with a photoionization rate of Γ_{-12}, expressed in units of $10^{-12}\,\mathrm{s}^{-1}$. Measurements find $\Gamma_{-12} \approx 1$ (e.g., Faucher-Giguère et al. 2008). The $T_4^{-0.7}$ factor arises because of the temperature dependence of the H I fraction in photoionization equilibrium, and many of the effects studied here derive from this dependence.

The amount of Lyα absorption is determined by inhomogeneities in the gas density, the peculiar velocity field, the photoionization rate, and the gas temperature. The first two sources are the standard contributions that were included in most previous studies and that are primarily responsible for the statistical properties of the Lyα forest. Almost all Lyα forest studies also have assumed that the temperature follows a power-law relation in density parametrized as $T(\Delta_b) = T_0 \, \Delta^{\gamma-1}$ (or they have effectively assumed a power-law relation by using simulations with a spatially uniform ionizing background). This study focusses on the impact of temperature fluctuations around $T(\Delta_b)$, and it also considers fluctuations in the photoionization rate. In addition to modulating the amplitude of $\tau_{\mathrm{Ly}\alpha}$, inhomogeneous heating alters 10s of km s^{-1} absorption features via its impact on the gas pressure and on the thermal widths of absorption lines.

Large-scale temperature fluctuations should be present in the IGM as a relic of reionization processes. The reionization of hydrogen and helium were spatially inhomogeneous, with some regions ionized earlier and some later depending on their proximity to the ionizing sources. Models for these processes predict order unity fluctuations in the ionization fraction of the species being reionized on ∼ 10 Mpc scales and accompanying order unity fluctuations in the temperature (e.g., Trac et al. 2008; McQuinn et al. 2009). Temperature fluctuations should have been imprinted on the IGM during reionization because: (1) different regions in the IGM would have been ionized by different energy photons, and (2) a gas element's instantaneous temperature depends on its ionization history. Once a typical element was reionized and heated, it would have subsequently cooled adiabatically owing to the expansion of the Universe (with Compton cooling off of the CMB and line cooling playing a minor role). This cooling proceeded until the gas element reached the temperature at which heating from ionizations of the residual bound electrons balanced the cooling from expansion (Miralda-Escudé & Rees 1994; Hui & Gnedin 1997;

Theuns et al. 2002). At this point, the temperature difference with initially cooler elements would have been erased. At $z < 6$, it takes on the order of a Hubble time to erase temperature fluctuations.[1]

The Lyα forest indicates that hydrogen was likely reionized at $z > 6$. For any physical radiation spectrum that reionized the hydrogen, the intergalactic helium would have been at least singly ionized simultaneously with the hydrogen. At $z < 4$, the relic temperature fluctuations from $z > 6$ reionization processes would have largely faded away (Hui & Gnedin 1997; Trac et al. 2008). However, a hard source of ionizing photons is required to doubly ionize helium (normal stars cannot do it). The current paradigm is that the intergalactic helium was doubly ionized by the radiation from quasars at $z \sim 3$ (Davidsen et al. 1996; Schaye et al. 2000; Agafonova et al. 2007; McQuinn 2009; Becker et al. 2011; Shull et al. 2010; Furlanetto & Dixon 2010; Dixon & Furlanetto 2009). Models predict that at $z \approx 3$ He II reionization would have imprinted large inhomogeneities in the temperature, much larger than those remaining from hydrogen reionization (Furlanetto & Oh 2008b; McQuinn et al. 2009).

2.1 Simulations of the IGM Temperature

Using radiative transfer simulations, McQuinn et al. (2009) made predictions for the level of intergalactic temperature fluctuations expected during He II reionization. These simulations are employed extensively in our new study. In these simulations, the first regions in which the He II was reionized were closest to quasars and, therefore, were ionized by softer photons and heated by less than 10^4 K. These regions subsequently cooled with the expansion of the Universe. Whereas, the last regions to be ionized were more significantly heated by ionizations from a hardened radiation background. Thus, the temporal extent of this process resulted in large fluctuations in the intergalactic temperature. See Abel & Haehnelt (1999) for discussion of relevant radiative transfer effects.

Figure 1 shows slices through three snapshots of a 430 Mpc He II reionization simulation from McQuinn et al. (2009). The left panels are the He III fraction, the middle panels are the temperature, and the right panels are the change in the Lyα forest transmission relative to the case with the same mean relation between T and Δ_b, but without temperature fluctuations. By the end of He II reionization in this simulation, the temperature at the cosmic mean density fluctuated between 10 and 30 kiloK, resulting in $\approx 10\%$ fluctuations in the Lyα forest transmission.

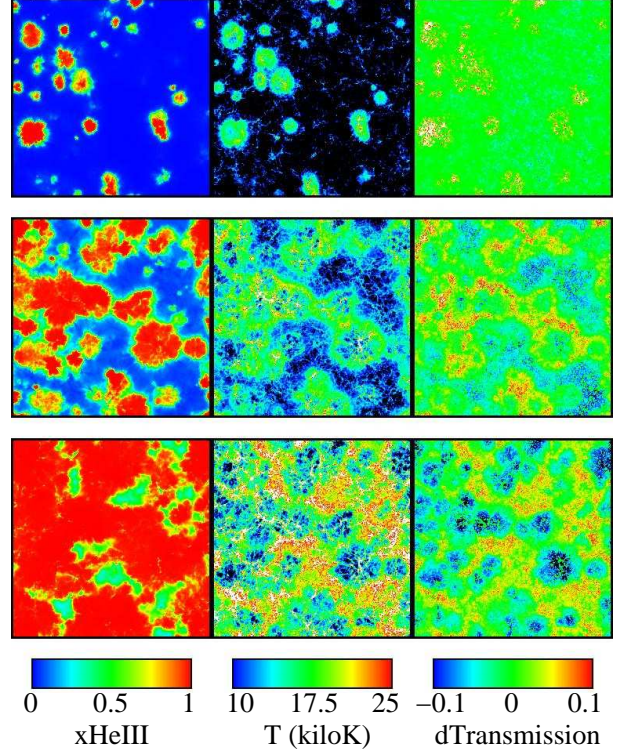We briefly summarize the characteristics of the temperature fluctuations in these simulations, but see

[1] To quantify this, we have solved for the evolution of T_0 as in Hui & Gnedin (1997) after hydrogen and helium reionization, assuming a flat specific intensity at the H I, He I, and He II ionization edges (but the results depend weakly on this assumption). If half of the gas were at $T_0 = 15,000$ K and half at $T_0 = 25,000$ K at $z = 3$, by $z = 2$ the amplitude of fluctuations in T_0 would have been 70% of what they had been, half at $17,000$ K and half at $12,000$ K. If instead half the IGM were at $T_0 = 15,000$ K and half at $T_0 = 25,000$ K at $z = 4$, the amplitude of temperature fluctuations at $z = 2$ would have been reduced to 40% of its initial value.

Figure 1. Slices through simulation B1 from McQuinn et al. (2009). The left panels show the He III fraction, the middle panels the temperature, and the right panels deviations in the transmission relative to the case without temperature fluctuations but with the same mean $T(\Delta_b)$. Each panel is $430\,\mathrm{Mpc} \times 430\,\mathrm{Mpc} \times 8\,\mathrm{Mpc}$ in size, with (from top to bottom) volume-averaged He II fractions of $\bar{x}_{\mathrm{HeII}} = 0.1, 0.5$, and 0.9 at $z = 5$, 4, and 3.5, respectively.
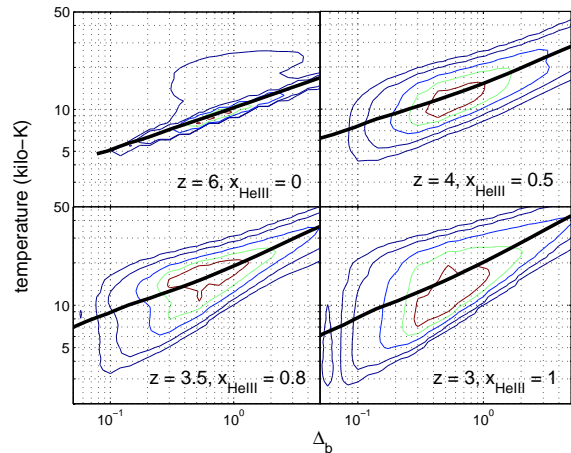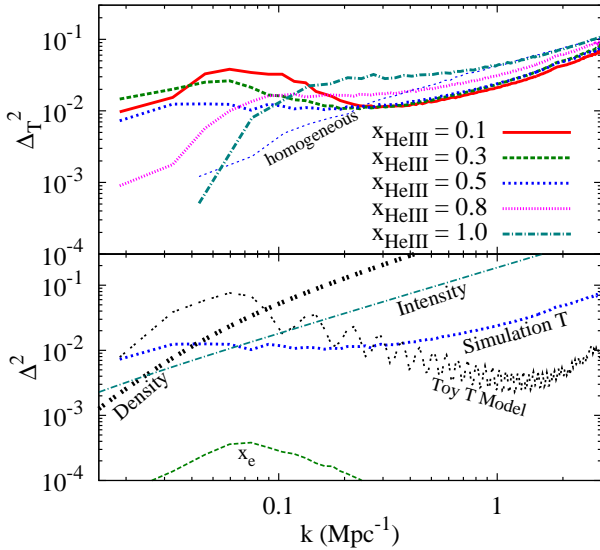

Figure 2. Distribution of gas elements in the T-Δ_b plane from the D1 simulation in McQuinn et al. (2009), a smaller box version of the simulation featured in Figure 1. The thick solid curves are the mean $T(\Delta_b)$, and the contours enclose $33, 67, 90, 99$, and 99.9% of the grid cells. These contours enclose the regions that have the highest density of gas elements in $\log T$ - $\log \Delta_b$.

Figure 3. Top Panel: Magnitude of temperature fluctuations, quantified in terms of the dimensionless power spectrum, $\Delta_T^2 \equiv k^3 P_T/2\pi^2$, where P_T is the power spectrum of $\delta_T \equiv T/\bar{T} - 1$. The thick curves show Δ_T^2 for different He III fractions in the fiducial simulation of He II reionization. The thin blue dotted curve labeled "homogeneous" assumes $\gamma \approx 1.6$ and $T_0 \approx 10^4$ K. Bottom Panel: $\Delta^2 \equiv k^3 P_X/2\pi^2$, where P_X is the power spectrum of the overdensity in X. The blue dotted curve is for the same temperature model as in the top panel, and the curve labeled "Toy T Model" is Δ_T^2 for $\gamma - 1 = 0.3$, where half the IGM is filled with uncorrelated 30 Mpc spheres with $T_0 = 20,000$ K and the other regions have $T_0 = 10,000$ K. The dashed green curve labeled x_e is Δ^2 for electron fraction fluctuations, and the curve labeled "Density" is this for density fluctuations.

McQuinn et al. (2009) for additional details. The solid curves in Figure 2 show the mean temperature as a function of Δ_b at different times in a higher resolution version of the simulation in Figure 1. All of these curves can be approximated by a power-law temperature density-relation with $\langle \gamma - 1 \rangle \approx 0.35$. However, there is significant scatter around this relation, with the scatter increasing as He II reionization proceeds. Moreover, the scatter is larger at lower Δ_b, a property that affects the observability of these fluctuations (Section 4). The contours in Figure 2 enclose 33, 67, 90, 99, and 99.9% of the grid cells.

The top panel in Figure 3 plots the dimensionless 3D power spectrum of temperature fluctuations, calculated from different times during the He II reionization simulation. We use the notation $\Delta_X^2 \equiv k^3 P_X(k)/2\pi^2$, where P_X is the power spectrum of the overdensity in X. The power law-like scaling of Δ_T^2 at $k \gtrsim 1$ Mpc^{-1} owes to the temperature fluctuations being highly correlated with the small-scale density fluctuations because of adiabatic cooling and heating. The shape of Δ_T^2 at $k \lesssim 1$ Mpc^{-1} owes to the large-scale inhomogeneous heating during He II reionization (top panel, Figure 3). Fluctuations at the $\sim 10\%$ level are present even for the largest modes in our 430 Mpc box during the bulk of He II reionization.

The bottom panel in Figure 3 compares Δ_T^2 from the snapshot with $x_{\rm HeII} = 0.5$ (dotted curve) with other relevant

sources of fluctuations. A common toy model for IGM temperature fluctuations takes half of the IGM to be at 10 kiloK and the other half to be at 20 kiloK. The curve labeled "Toy T Model" is such a model, in which 30 Mpc, 20 kiloK bubbles are placed randomly until they fill half of the volume. The ringing behavior owes to the artificial top-hat bubble morphology. The fluctuations in this model are a few times larger than in the simulation. Thus, a similar level of temperature fluctuations as in the simulations should be more difficult to detect than in this model. This is an important point because Theuns et al. (2002) and Lidz et al. (2010) found they could rule out this toy model using a wavelet analysis (Section A1). The curve labeled "Density" is $k^3 P_\Delta(k)/2\pi^2$ at $z = 3$, where the non-linear density power-spectrum $P_\Delta(k)$ is calculated using the Peacock & Dodds (1996) fitting function. The temperature fluctuations in the simulation can be as large as the density fluctuations at the smallest k captured, which suggests that such temperature fluctuations would have a significant effect on the large-scale transmission fluctuations.

He II reionization also produces additional free electrons, increasing the electron abundance (and $\tau_{\rm Ly\alpha}$) by 8% in He III regions. The power spectrum of the electron fraction from the $\bar{x}_{\rm HeII} = 0.5$ snapshot is represented by the dashed green curve in the bottom panel in Figure 3. The temperature fluctuations in the simulation are almost an order of magnitude larger than the fluctuations in x_e.

An inhomogeneous ultraviolet background (which modulates Γ_{-12}) is the final potential nonstandard source of transmission fluctuations in the forest and is also the most studied (Zuo 1992a,b; Meiksin & White 2004; Croft 2004; McDonald et al. 2005; Furlanetto 2009; Mesinger & Furlanetto 2009; White et al. 2010). The curve labeled "Intensity" represents an empirically motivated model for intensity fluctuations at $z = 3$ (see Section 5). Thus, the intensity power can also be comparable to that in the density at the smallest k.

3   METHODOLOGY

We use two of the He II reionization simulations presented in McQuinn et al. (2009). The radiative transfer calculation in these simulations was run on a 256^3 grid in post-processing using the density field from either a 190 or 430 Mpc cosmological N-body simulation. Both simulations employ the same model for the sources. In addition to the He II reionization simulations, we use three supplementary simulations, all initialized with different random seeds. We use a 4000^3 N-body simulation described in White et al. (2010). This simulation has dimensions of 750 Mpc/h and the dynamics were softened at 100 kpc/h to approximate pressure smoothing for $\sim 10^4$ K gas. The other two supplementary simulations are 25 Mpc/h Gadget-2 runs (Springel 2005) described in Lidz et al. (2010) with either 512^3 or 1024^3 dark matter and SPH particles. The supplementary simulations are used to overcome the resolution and sample variance limitations of the He II reionization simulations, as well as to include hydrodynamical effects absent in the reionization simulations. All of these simulations were initialized with cosmological parameters that are consistent with the measurement of Komatsu et al. (2011).

We add fluctuations in the temperature to the supplementary simulations using both toy models and a method that employs the temperature information from the He II reionization simulations. The latter method relies on the property that locally the T–Δ_b relation is well-approximated by a power law even though globally a power law is a poor approximation. A local power law holds because neighboring cells have roughly the same thermal history. Specifically, this method obtains T_0 and γ for a cell in the He II reionization simulation by fitting this power-law model to T and Δ_b in the surrounding 5^3 cells, and it does this along one long diagonal skewer that cycles through the He II reionization simulation box. It then uses the resulting T_0 and γ to transfer the temperature field to density and velocity skewers extracted from the supplementary simulations (which we make periodic with length equal to the box size).

Figure 4 examines the validity of this method. The three sets of 5^3 points with different markers represent the values of T and Δ_b for the cells in three randomly selected regions of size 3.6 Mpc in the fiducial He II reionization simulation. The lines are the best-fit power law to each set of points. We find that $\Delta T / T \approx 0.1 - 0.2$ is typical of the error around the best-fit $T - \Delta_b$ relation, which is much smaller than the global dispersion in the temperature. Thus, the local power-law approximation appears to be justified. However, this method assumes that the correlations between the large-scale temperature and density modes are unimportant. This is motivated by the fact that the correlation between temperature and large-scale density is weak in the reionization simulations owing to the rare nature of the sources. We will elaborate on the applicability of this approximation later.

We will often use our method to add the He II reionization simulation temperature field at one redshift to a snapshot in the supplementary simulations from another redshift. This makes possible visual comparison of how the temperature fluctuations affect the statistic in question throughout the reionization process without the confusion of cosmological evolution in the density field. In addition, there is uncertainty in exactly when He II reionization by quasars would have occurred: Lidz et al. (2010) argued from the inferred temperature history that the end was at $z \approx 3.5$. Whereas, McQuinn (2009) and Shull et al. (2010) argued that it was not complete until at least $z = 2.7$, citing the presence of He II Lyα Gunn-Peterson troughs down to this redshift.

4 STATISTICS

4.1 Small-scale Line-of-Sight Power Spectrum

The line-of-sight power spectrum of transmission fluctuations is the principle statistic that has been used to derive cosmological constraints from the Lyα forest. Here we investigate how temperature fluctuations affect this statistic at $k \sim 0.1 \, \mathrm{s \, km^{-1}}$, and Section 4.3 examines larger scales. Studies of the forest marginalize over T_0, γ, and (in some cases) the reionization redshift to derive cosmological constraints, but the impact of the thermal history has the potential to be more complicated.

Thermal broadening is the most important temperature-dependent effect on the small-scale power spectrum. Pressure smoothing of the gas can also smooth
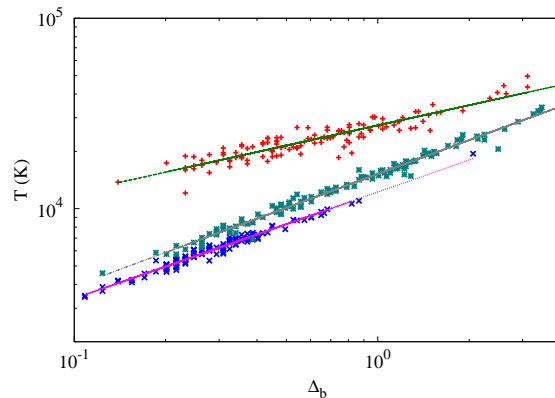

Figure 4. Fits to the local T–Δ_b relation using the $z = 3.0$ snapshot from the 190 Mpc He II reionization simulation. The lines represent the best-fit T–Δ_b relation in 3 separate, randomly selected regions of 5^3 cells (corresponding to 3.6 Mpc on a side). The markers represent the value of T and Δ_b in each set of 5^3 cells.

out the small-scale transmission fluctuations. However, pressure effects are not included self-consistently in any of the simulations analyzed here. There are physical arguments for why pressure smoothing is less important to include than thermal broadening:

(i) Gnedin & Hui (1998) showed analytically that in an expanding universe the scales at which pressure damps the growth of linear modes are a couple times smaller than the Jeans wavelength and smaller than the scale at which thermal broadening erases fluctuations. Both Gnedin & Hui (1998) and Peeples et al. (2010) confirmed with simulations that thermal broadening dominates the exponential damping of the small-scale power in the forest.

(ii) The timescale for a typical Lyα forest absorber to relax to equilibrium after a heating event is comparable to the Hubble time (Gnedin & Hui 1998). During He II reionization, the additional pressure smoothing from the associated heating would not have had a significant effect on the statistics of the forest if this heating occurred within a redshift interval of $\Delta z \approx 2$ (see Fig. 29 in Lidz et al. 2010).

Heating will also induce velocity gradients that broaden the majority of absorption systems (Theuns et al. 2000). The effect of this broadening mechanism on the Lyα forest power-spectrum has not been quantified in as much detail. This process is unlikely to lead to an exponential cutoff in the small-scale power like thermal broaden because systems with zero width in redshift-space after including this process can still exist.

Thus, this study ignores the dynamical response of the gas, a common approximation in such analyzes. However, this may bias the interpretation in this section and that in Section A1 towards favoring higher temperatures. A treatment that includes this effect would be challenging.

The shape of small-scale Lyα forest power spectrum is sensitive to the average temperature as well as the temperature distribution. If f_1 of the volume is at temperature T_1 and the rest is at temperature T_2, thermal broadening results in the small-scale power spectrum achieving the lim-
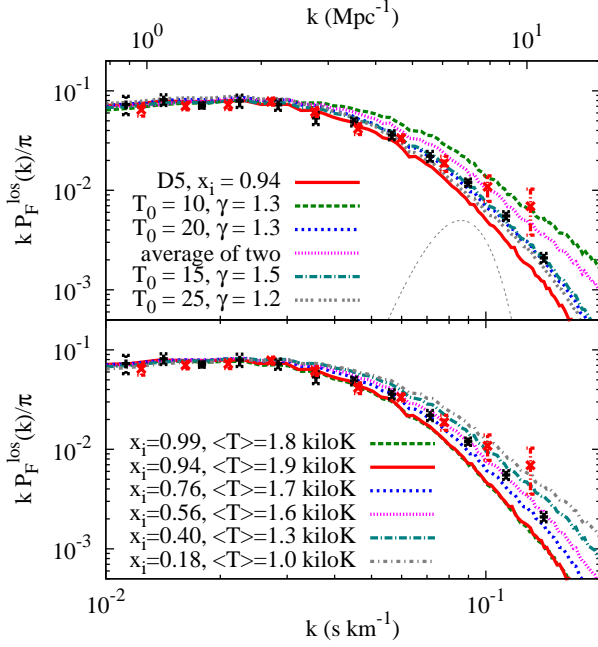
Figure 5. Top panel: The line-of-sight power spectrum of δ_F at $z = 3$ calculated from the 2×512^3 particle 25 Mpc/h simulation and focussing on the small scale affected by thermal broadening. The D5 curve is from the fiducial He II reionization simulation, the other curves are power-law $T - \Delta_b$ models, and the "average of two" curve is the average of the 10 kiloK and 20 kiloK models with $\gamma = 1.3$. Bottom panel: $P_F^{\rm los}$ at $z = 3$ calculated using the temperature field from different simulation snapshots, labeled by their He III fraction (x_i in the plot). In both panels, the black points with error bars are the measurement of McDonald et al. (2000) and the orange are the measurement of Croft et al. (2002). The temperature field is taken from the snapshots at $z = 2.7, 3, 3.3, 3.6, 4$, and 4.5 in the simulation. The thin Gaussian curve in the top panel is the wavelet filter used in Appendix A, arbitrarily normalized.

iting form at high k of

$$P_F^{\rm los}(k) \rightarrow f_1 \exp\left(-a\, T_1\, k^2\right) + (1 - f_1) \exp\left(-a\, T_2\, k^2\right), \quad (2)$$

where $a = 2k_b/m_p$. In the limit that $T_2 > T_1$ and $a\, T_2\, k^2 \gg 1$, the power spectrum is solely determined by the regions with T_1.

An additional consideration is that the small-scale power at $z \sim 3$ is dominated by slightly overdense regions because these are the regions that contribute the narrowest absorption lines. At $z = 3$, simple tests show that power on the exponential tail of $P_F^{\rm los}$ is primarily from regions with $\Delta_b \approx 2-3$, and this characteristic density decreases with increasing redshift. The dispersion in the temperature resulting from an inhomogeneous reionization process should be smaller in overdense regions than in underdense ones. This trend is evident in the simulations (Fig. 2), and it acts to reduce the impact of temperature fluctuations on the small-scale shape of $P_F^{\rm los}$.

Figures 5 and 6 plot the small-scale line-of-sight power spectrum of δ_F for several temperature models at $z = 3$ and $z = 4$, respectively. All curves were calculated from the $25/h$ Mpc Gadget-2 simulations (Section 3), and the points with error bars are the measurements of McDonald et al. (2000) and Croft et al. (2002). In the top panels, the green
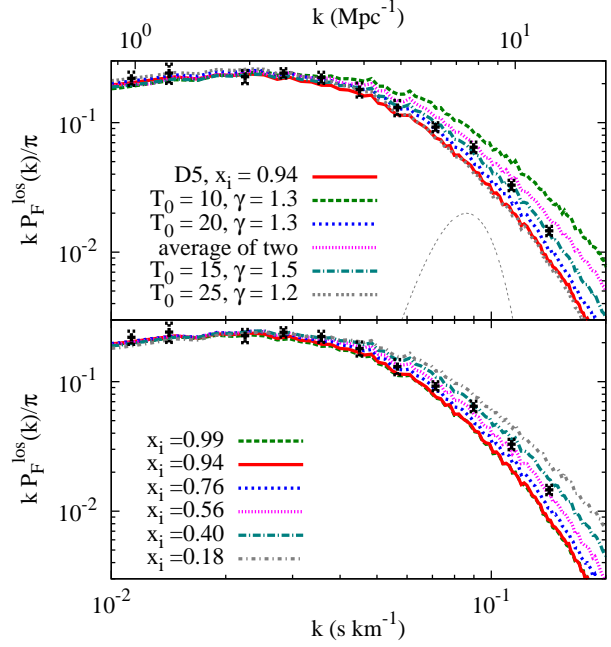

Figure 6. Same as Figure 5 but for $z = 4$ and calculated from the 2×1024^3 particle simulation. See the key in Figure 5 for the mean temperature of the reionization simulation model curves.

dashed (blue dotted) curves are for an IGM with $\gamma = 1.3$ and $T_0 = 10$ kiloK (20 kiloK). If $\gamma = 1.3$ and half of the IGM had $T_0 = 10$ kiloK and the other half $T_0 = 20$ kiloK, then the small-scale power spectrum would be given by the magenta dotted curve, which has a slightly flatter shape than the single T_0–γ models. The the shape of this curve appears to be inconsistent with the McDonald et al. (2000) data. However, a toy model for the temperature field that is better motivated by the He II reionization simulations is half of the IGM at $T_0 = 15$ kiloK with $\gamma = 1.5$ and half at $T_0 = 25$ kiloK with $\gamma = 1.2$. The difference in the small-scale power spectrum between these two states is negligible. (Compare the teal dot-dashed and grey quadruple-dotted curves in the top panels.) Therefore, the fluctuations in this toy model would not be detectable in $P_F^{\rm los}$.

The bottom panels in Figures 5 and 6 are the power spectrum of models that use the temperature field of different snapshots from the 190 Mpc He II reionization simulation. The IGM is gradually heated throughout He II reionization, which results in the small-scale power decreasing with time, or equivalently, with He III fraction. The amount of evolution is sensitive to the simulation's initial conditions, especially with decreasing $\bar{x}_{\rm HeIII}$. This simulation was initialized with $T_0 = 10$ kiloK and $\gamma = 1.3$ at the starting redshift of $z = 6$. If the simulation were instead initialized with $T_0 = 15$ kiloK, there would have been less evolution.

At the end of He II reionization, the simulation temperature reaches values that are slightly hotter than suggested by the $z = 3$ measurements of McDonald et al. (2000) and Croft et al. (2002). The $x_{\rm HeIII} = 0.94$ curve in Figure 5 corresponds to $z = 3$ in the simulation. The measurement of McDonald et al. (2000) at $z = 4$ in Figure 6 appears to be more consistent with *slightly* cooler temperatures than their
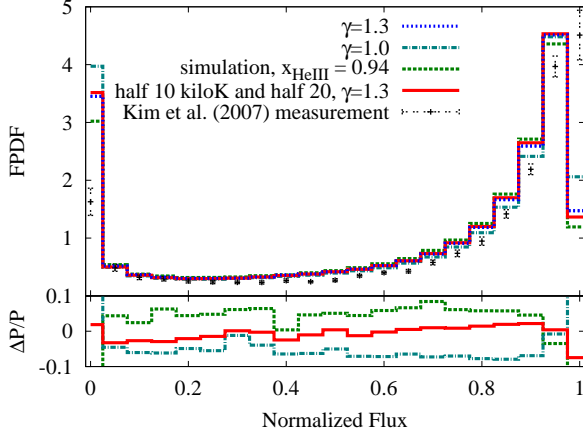
Figure 7. Top panel: The PDF of the normalized flux. The blue dotted curve represents a model with $\gamma = 1.3$, and the teal dot-dashed curve for $\gamma = 1.0$. The red solid curve represents a model with $\gamma = 1.3$, but where half the IGM has $T_0 = 10$ kiloK and the other half $T_0 = 20$ kiloK. The green dashed curve is this PDF for the temperature field from the He II reionization simulation. The points with errorbars are the measurement of Kim et al. (2007). Bottom Panel: The relative difference between the flux PDF in these temperature models and in the $\gamma = 1.3$ model.

$z = 3$ measurement. For reference, the $x_{\mathrm{HeIII}} = 0.4$ output is at $z = 4$ in the reionization simulation.

There are several systematics that may bias these interpretations. The observations are biased in the direction of having extra power by instrumental noise and especially by metal lines, and the simulations are also biased in the direction of extra power as previously described because pressure smoothing is not properly captured and the simulation gas temperatures (prior to our post-processing) are on the low side. Lidz et al. (2010) estimated that pressure smoothing could alter the power at $k \sim 0.1$ s km^{-1} by a maximum of 20% (see their Fig. 29), but its impact should be significantly smaller for the He II reionization scenarios considered here where the heating has been more recent than in this case in Lidz et al. (2010). Uncertainties in the mean flux are also important for the comparison at $z = 4$ (Lidz et al. 2010).

In conclusion, measurements of the small-scale Lyα forest power spectrum reveal that $15 < T_0 < 25$ kiloK at $z = 3$, with tentative evidence for an decrease in temperature from $z = 3$ to 4 in the McDonald et al. (2000) measurement. However, finer determinations would be challenging because the systematics are at the level of the model differences. We also find that it would be difficult to detect physically motivated models for temperature fluctuations with this statistic.

Appendix A considers the impact of the temperature models considered here on wavelet statistics. Wavelets are also a measure of the small-scale power in the forest, and are better suited than the small-scale behavior of P_F^{los} for detecting temperature inhomogeneities. Despite this advantage, Appendix A reaches similar conclusions to this section.

4.2 Flux Probability Distribution

Another statistic that is often applied to the Lyα forest is the probability distribution function of the normalized flux (FPDF). A distribution of temperatures at a given Δ_b will

broaden the FPDF relative to the case of a single $T - \Delta_b$ relation. In fact, measurements of the FPDF have claimed to find too many hot voids at $2 < z < 3$ compared to cosmological hydrodynamic simulations with standard, homogeneous thermal histories. This led Bolton et al. (2008) and Viel et al. (2009) to argue that an inverted $T - \Delta_b$ relation ($\gamma - 1 < 0$) was needed to reconcile this discrepancy. He II reionization by the observed population of quasars cannot generate an inverted relation (McQuinn et al. 2009). However, perhaps an inverted relation is not required to explain the data, but may rather be accounted for by additional dispersion in the temperature as conjectured in McQuinn et al. (2009). Dispersion would have made some of the voids hotter and, as a result, more transparent to Lyα photons.

The top panel in Figure 7 plots the FPDF at $z = 3$. The points with errorbars are the measured FPDF from Kim et al. (2007). The curves are this statistic calculated from 1000 skewers through the $25/h$ Mpc simulation. The red solid curve represents a toy model in which $\gamma = 1.3$ and where half the IGM has $T_0 = 10$ kiloK and the other half $T_0 = 20$ kiloK. The green dashed curve was calculated using the temperature at the end of the He II reionization simulation (where $x_{\mathrm{HeIII}} = 0.94$), and corresponds to the simulation snapshot in which the dispersion in temperature is approximately maximized. The blue dotted curve represents a model with $\gamma = 1.3$ and with T_0 equal to the average in the $x_{\mathrm{HeIII}} = 0.94$ snapshot. However, the dependence of this curve on T_0 is weak. The bottom panel in Figure 7 plots the relative difference between the $\gamma = 1.3$ model and the other temperature models featured in the top panel.

We next estimate the magnitude by which temperature fluctuations alter the FPDF. To proceed, we write the FPDF, $\mathcal{P}$, as a Taylor expansion in δ_{Tp7}:

$$\mathcal{P}(F) \approx \tilde{\mathcal{P}}(F) + A\langle \delta_{Tp7} \rangle + B\langle \delta_{Tp7}^2 \rangle + ..., \qquad (3)$$

$$A \equiv \frac{d\tilde{\mathcal{P}}}{dF}\tilde{F}\tau - \mathcal{P}(1 - \tau),$$

$$B \equiv \frac{d^2\tilde{\mathcal{P}}}{dF^2}\tau^2\tilde{F}^2 - \frac{d\tilde{\mathcal{P}}}{dF}\tilde{F}(4\tau - 3\tau^2) + \mathcal{P}(2 - \tau[4 - \tau]),$$

where $\tilde{\mathcal{P}}$ is the FPDF without temperature fluctuations, δ_{Tp7} is the fluctuation in $T^{-0.7}$ around the average T-Δ_b relation, $\tilde{F}$ is flux for the average T-Δ_b relation, $\langle ... \rangle$ represents an average at $\tilde{F}$ (roughly corresponding to fixed Δ_b), and $\tau \equiv -\log(\tilde{F})$. Both A and B are of the order of $\mathcal{P}(F)$, and we find $A \approx 0.3$ and $B \approx -0.1$ at $F = 0.7$. The leading order contribution from temperature fluctuations *about the mean* $T - \Delta_b$ *relation* is $B\langle \delta_{Tp7}^2 \rangle$. Plugging in $\langle \delta_{Tp7}^2 \rangle \sim 0.2^2$, which is characteristic of the simulation temperature model at $F \approx 0.7$, we estimate that temperature fluctuations should alter $\mathcal{P}(F)$ at the several percent level.

The size of the residuals in the bottom panel of Figure 7 qualitatively agree with the above estimate that temperature fluctuations should produce a percent-level change in $\mathcal{P}(F)$. The predictions are not in quantitative agreement (and sometimes has the incorrect sign) because we have not included the normalization to a single mean flux in our analytic expressions, which fixes the first moment of the FPDF. We conclude that a different effect is required to create the $\approx 20\%$ *suppression* of the FPDF that Bolton et al. (2008) finds at $F \approx 0.7$. Additional dispersion in the temperature

(even with a much larger amplitude than in our He II reion-ization simulations) is unable to explain the discrepancy between the observed and simulated FPDFs.

Changing γ can have a larger effect on the FPDF than adding dispersion to the temperature because, in this case, the leading order term is $A \langle \delta_{Tp7} \rangle$. (Compare the $\gamma = 1.3$ with the $\gamma = 1.0$ curve in Figure 7.) Performing a more detailed comparison than considered here, Bolton et al. (2008) found that an inverted relation with $\gamma \approx 0.5$ provided the best fit to the Kim et al. (2007) FPDF measurement. However, an inverted relation may not be the only explanation and would require an unknown heating mechanism. The FPDF is especially sensitive to the accuracy of continuum fitting (Lee 2011) and the efficacy of metal-line removal.

4.3   Large-Scale Correlations

The remainder of this paper discusses large-scale correlations in the Lyα forest. At scales where $\delta_F \equiv F/\bar{F} - 1$ and δ_T are small, the 3D power spectrum of δ_F can be expressed as bias factors times the power spectra of the different sources of fluctuations. In particular,

$$P_F(\boldsymbol{k}) \approx b^2 \Big(G^2 P_\Delta(k) + 2 G \epsilon^{-1} \left[P_{\Delta\, Tp7}(k) - P_{\Delta\, J}(k) \right]$$

$$+ \epsilon^{-2} \left[P_{Tp7}(k) + P_J(k) \right] \Big), \tag{4}$$

where $\boldsymbol{k}$ is the Fourier wavevector, $k = |\boldsymbol{k}|$, $Tp7$ is shorthand for the temperature field to the -0.7 power, J represents intensity, $P_{\Delta\, X}(k)$ is the cross power spectrum between density and the overdensity in X, $\mu = \hat{\boldsymbol{k}} \cdot \hat{n}$ where $\hat{n}$ is the line-of-sight direction, and $\epsilon \approx 2 - 0.7 (\gamma - 1)$. The $G \equiv (1 + g\mu^2)$ factors arise from peculiar velocities (Kaiser 1987), and g reflects that these distortions have a different bias than density fluctuations. Our simulations require $g \approx 1$ (Appendix B).

The ϵ and ϵ^2 suppression of T- and J-dependent terms is approximate and results because the flux depends on Δ_b, T, and J via the combination $\Delta_F^\epsilon T^{-0.7} J^{-1}$. This suppression holds in linear theory, but can be violated by higher order correlations. Equation (4) suggests that at scales where either P_{Tp7} or P_J are comparable to P_Δ, these fluctuations can have a large effect on P_F.

4.3.1   Line-of-sight Correlations

Previous Lyα forest correlation analyses have primarily focused on the line-of-sight power spectrum and neglected correlations between sightlines. The line-of-sight power spectrum P_F^{los} can be expressed in terms of the 3D power spectrum P_F as

$$P_F^{\text{los}}(k_\parallel) = \int_{k_\parallel}^\infty \frac{dk}{2\pi} k\, P_F(k, k_\parallel/k), \tag{5}$$

where $k_\parallel$ is a line-of-sight wavevector. Because $\mu \equiv k_\parallel/k$, the projection to 1D suppresses the impact of large-scale peculiar velocities (and the $P_{\Delta X}$ terms; c.f. eqn. 4). In addition, 3D wavevectors with even $k \gg k_\parallel$ still contribute to P_F^{los} at $k_\parallel$. Figure 8 illustrates this aliasing effect, plotting at several $k_\parallel$ the fractional contribution per $\log k$ to P_F^{los} from different 3D modes with wavevector k. The red thick dashed curve represents this for $k_\parallel = 10^{-1}$ Mpc^{-1} and $g = 0$ (the
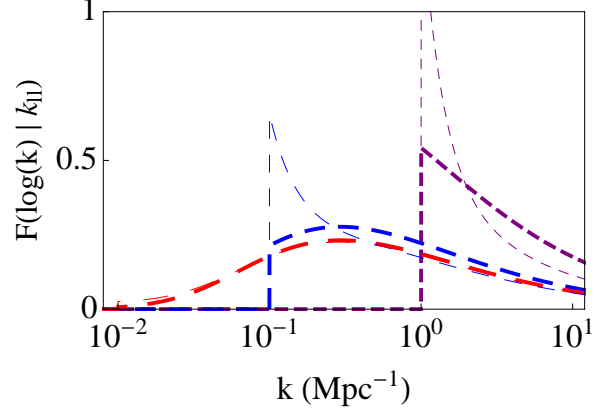

Figure 8. Fractional contribution per $\log k$ to P_F^{los} from different 3D wavevectors with modulus. The curves (in order of decreasing dash length) are $k_\parallel = 10^{-2}$, 10^{-1}, and 1 Mpc^{-1}. The thick curves are for $g = 0$ (no peculiar velocities) and the thin are for $g = 1$.
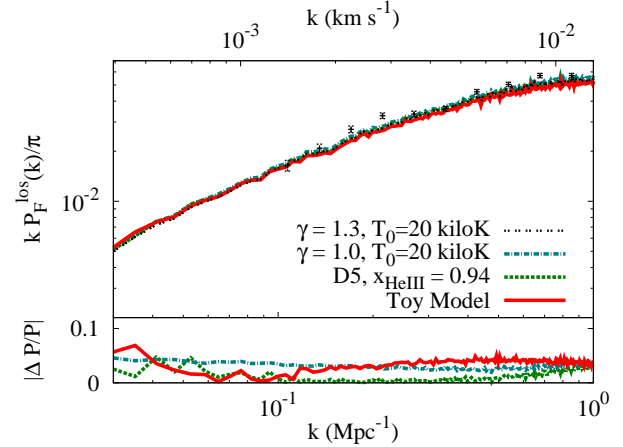

Figure 9. The large-scale line-of-sight dimensionless power spectrum for different temperature models at $z = 2.8$ (top panel), and the relative difference between these models and the $\gamma = 1.3$ model (bottom panel). The "Toy Model" curve assumes that $\gamma = 1.3$ locally and that 30 Mpc spheres with $T_0 = 20$ kiloK fill half of the volume and the rest is at $T_0 = 10$ kiloK. The error bars are the SDSS measurement presented in McDonald et al. (2005).

red thin dashed this for $g = 1$), approximately the value of the *3D* wavevector where P_T is maximized relative to P_Δ in some of our models (Fig. 3). Thus, $P_F^{\text{los}}(k_\parallel)$ receives a significant contribution from approximately two decades in k. This aliasing dilutes the impact of large-scale temperature fluctuations.[2]

Figure 9 quantifies the impact of temperature fluctuations on the line-of-sight power spectrum. The curves

---

[2] The calculations in Figures 8 assume the simple form $P_F(k, k_\parallel) = b^2 \left[1 + g\,(k_\parallel/k)^2 \right]^2 P_\Delta^{\text{lin}}(k) \exp[-k_b T k_\parallel^2/m_p]$, where P_Δ^{lin} is the linear theory overdensity power. We take $g = 1$ and $T = 20,000$ K. We find that this functional form provides a decent approximation to the spectrum of P_F in our simulations.

are $P_F^{\rm los}$, calculated using $22,500$ skewers of side-length 750 Mpc/h from the $z = 2.8$ snapshot of Run 1 in White et al. (2010) and using different temperature models. Each curve represents a different model for the temperature. However, the values of $P_F^{\rm los}$ in all of the considered models differ by less than 10%. These small differences qualitatively agree with the results of Lai et al. (2006).

The points with errorbars in Figure 9 are the SDSS measurement from McDonald et al. (2005). The differences between the plotted models are comparable or smaller than the McDonald et al. (2005) errorbars. Thus, the impact of these temperature models almost certainly could not be detected in $P_F^{\rm los}$ once one marginalizes over the cosmology. Temperature fluctuations could bias cosmological parameter determinations from $P_F^{\rm los}$, but at no more than the few percent-level in the considered models.

The calculations in Figure 9 implicitly assume that the large-scale temperature fluctuations do not correlate strongly with the large-scale density modes due to our method for adding temperature fluctuations. This is not always a good approximation for the calculation that uses the He II reionization simulation temperature field. Accounting for these correlations would increase the difference with the D5 curve by approximately a factor of 2, as can be inferred from the discussion in the Section 4.3.2.

The next section discusses the 3D power spectrum of the flux, a statistic which avoids the aliasing issues in $P_F^{\rm los}$. We show that temperature models that have almost no effect on $P_F^{\rm los}$ can alter the 3D power spectrum of the flux at an order unity level.

4.3.2   3D Correlations

The Sloan Digital Sky Survey III's Baryon Oscillation Spectroscopic Survey (BOSS) aims to observe the Lyα forest in the spectra of 1.6×10^5 quasars over an area of 8000 deg^2. A future survey, BigBOSS, will push a magnitude fainter, increasing this sample by a factor of a few.[3] BOSS's high density of quasars will allow the first measurement of the 3D Lyα forest power spectrum. A major goal of this effort is to detect the baryon acoustic oscillation (BAO) features. The 3D power spectrum will also be useful for studying temperature and other nonstandard sources of fluctuations in the forest because it avoids the aliasing issues that diminish the impact of large-scale correlations in $P_F^{\rm los}$.

Figure 10 quantifies the effect of the temperature fluctuations in the He II reionization simulations on P_F. The thick set of curves are calculated from the 190 Mpc simulation, and the thin (shown in three of the panels) are from the 430 Mpc one. The different normalization of the curves in the two simulations results primarily because of the different redshifts of the snapshots. The redshift of the 430 Mpc simulation curves is $\Delta z \approx 0.3$ higher than the quoted redshift because He II reionization occurs slightly earlier in this simulation (owing to fewer recombinations in this simulation). When calculating these curves, we normalize to the observed mean flux at the respective redshift. The solid curves are Δ_F^2
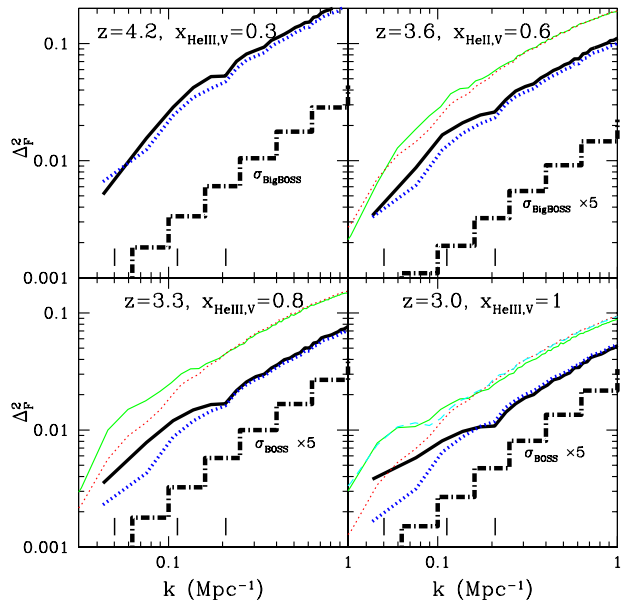
Figure 10. 3D Lyα forest dimensionless power spectrum. The dotted curves are calculated assuming $\gamma = 1.3$, and the solid curves adopt the temperature field predictions of the two He II reionization simulations. The thick curves are from the 190 Mpc simulation and are at the quoted redshift, and the thin curves (shown in three of the panels) are from the 430 Mpc simulation from a snapshot that is $\Delta z \approx 0.3$ higher. The vertical line segments mark the centers of the three BAO features that upcoming quasar surveys are targeting as a standard ruler. The bottom panels also include a piecewise curve representing the measurement error *multiplied by 5* of BOSS for the signal in each piecewise region as described in the text. The top panels include similar sensitivity curves but for BigBOSS. The cyan thin dashed curve in the bottom right panel also includes the prediction for Δ_F^2 in a toy temperature model that has 30 Mpc spheres at twice the temperature filling half of the volume.

computed using the temperature field from the He II reionization simulation at the quoted $x_{\rm HeIII}$ and, for comparison, the dotted curves show Δ_F^2 for a power-law $T - \Delta_b$ relation with $\gamma = 1.3$. Changing γ or T_0 has little effect on the latter curve.

Figure 10 illustrates that temperature fluctuations can significantly alter Δ_F^2 on large scales, changing its amplitude by as much as a factor of 2. In addition, the relative impact of temperature fluctuations at fixed $x_{\rm HeIII}$ largely agree between the small- and large-box simulations. This agreement is suggestive that the impact of temperature fluctuations on these scales is not affected by how well the small-scale features in the forest are resolved. The bottom right panel shows for comparison Δ_F^2 predicted for our toy model with 30 Mpc bubbles at twice the temperature filling half of space in the larger box (cyan thin dashed curve). Interestingly, even though the temperature fluctuations are much larger in this model than in the simulations (see Fig. 3), their effect on Δ_F^2 is comparable to that in the simulation temperature models.

The BOSS quasar survey is forecast to measure Δ_F^2 at $z \approx 3$ to $\sim 10\%$ accuracy in bins with $\Delta k \sim k$ in the range $10^{-2} < k < 1$ Mpc^{-1}, precision beyond what would be re-

quired to detect this extra power in some of our models. The bottom panels in Figure 10 includes an estimate discussed in McQuinn & White (2011) for the measurement error of BOSS *multiplied by 5*, assuming 8000 deg^{-2} over a region of depth 500 Mpc. These curves are calculated assuming $\bar{n}_{\rm eff} = 3 \times 10^{-4}$ Mpc^{-2} for the $z = 3$ panel and $\bar{n}_{\rm eff} = 2 \times 10^{-4}$ Mpc^{-2} for the $z = 3.3$ (corresponding to $\approx 2-3$ per deg^2), where $n_{\rm eff}$ is a noise weighted number density of quasars on the sky and defined in McQuinn & White (2011). The sensitivity scales as $n_{\rm eff}^{-1}$. These number densities take the quoted magnitude limit for BOSS of $m = 22$, assuming that all quasars below this magnitude are targeted and that $S/N = 1$ in 1 Å pixels at $m = 22$. With these assumptions, BOSS will be several times more sensitive to P_F at $z = 2 - 2.5$ compared to at $z = 3$. In addition, the vertical line segments in this figure mark the centers of the three BAO features that the BOSS and other upcoming quasar surveys are targeting as a standard ruler. Temperature fluctuations have the potential to bias the measurement of this feature unless a fairly general functional shape is assumed for the continuum on which these features sit.

BigBOSS aims to obtain a denser sample of quasars, and we forecast that it will be able to constrain Δ_F^2 to $z \approx 4$ if its survey strategy is similar to that of BOSS, and possibly to higher redshifts if this strategy is optimized to go deeper (McQuinn & White 2011). The dot dashed curves in the top panels in Figure 3 show what BigBoSS can achieve, assuming that it obtains spectra for quasars that are a magnitude fainter than BOSS such that $\bar{n}_{\rm eff} = 5 \times 10^{-4}$ Mpc^{-2} at $z = 2.6$ and 1×10^{-4} Mpc^{-2} at $z = 4.2$.

Peculiar velocities are not included in the calculation of the curves in Figure 10 and the gas is assumed to be in the Hubble flow. Peculiar velocities reduce the importance of temperature fluctuations. However, peculiar velocities do not contribute to the power in modes transverse to the line of sight, and, thus, we expect that the differences seen in Figure 10 should be representative of the effect on transverse modes and the monopole component of Δ_F^2. Observations will be most sensitive to the Δ_F^2 monopole (Section 6).

Figure 11 demonstrates that equation (4) provides a reasonable description of the impact of temperature fluctuations in the reionization simulations. This figure compares the predictions for Δ_F^2 from equation (4) (red dashed curve) with that of the full numerical result (black solid curve). The red dashed curve is constructed by adding each contribution that appears in equation (4) separately, and the value of b^2 in this equation was derived by taking the ratio of $\tilde{P}_F$ to P_Δ. The blue dotted curve is Δ_F^2 for a power-law $T - \Delta_b$ relation with $\gamma = 1.3$, the green long dashed curve and thick cyan dot-dashed are respectively $(b/\epsilon)^2 \Delta_{Tp7}^2$ and $2b^2/\epsilon \Delta_{Tp7\Delta}^2$. (The thin cyan curves are $-2b^2/\epsilon \Delta_{Tp7\Delta}^2$.) The field δ_{Tp7} is taken to be the overdensity in temperature around the mean $T - \Delta_b$ relation, a slightly different definition than used previously and that is motivated in Appendix C. The sum of the blue dotted, green long dashed, and $\pm$ the cyan dot-dashed curve yields the red dashed curve, which is remarkably similar to the black solid curve. (See Appendix C for a complementary analytic description of the impact of temperature fluctuations.)

The history of $P_{Tp7\Delta}$ in the He II reionization simulation is complicated. This function is less than zero at the beginning of He II reionization and at the largest-scales be-
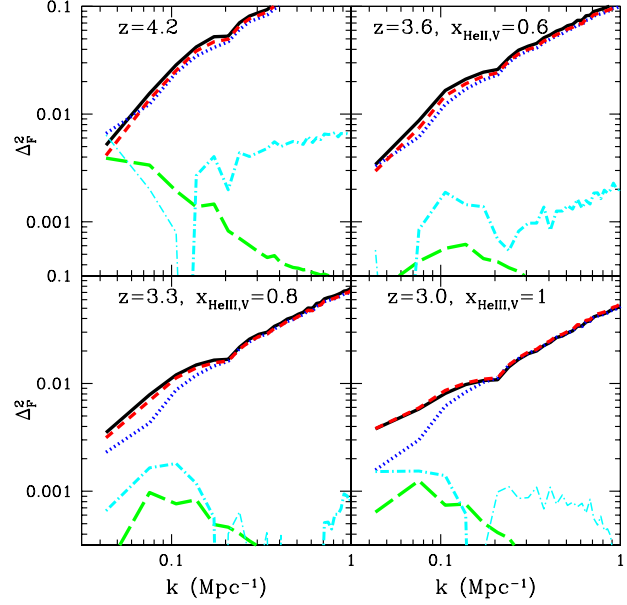

Figure 11. Comparison of the predictions for Δ_F^2 using equation 4 (red dashed curves) and the full numerical result from the 190 Mpc box (black solid curves). The blue dotted curves are Δ_F^2 for a power-law $T - \Delta_b$ relation with $\gamma = 1.3$, and the green dashed curves and cyan dot-dashed curves are respectively the contribution proportional to P_{Tp7} and $|P_{Tp7\Delta}|$. In particular, the thin cyan dot-dashed curves are $-2b\epsilon^{-1}P_{Tp7\Delta}$ and the thick are $2b\epsilon^{-1}P_{Tp7\Delta}$. In each panel, the sum of the blue, green, and $\pm$ the cyan dot-dashed curve yields the red dashed curve.

cause quasars are heating their immediate surroundings (top left panel, Fig. 11). Later, it becomes positive as the large-scale void regions are ionized. Constraining this nontrivial evolution from observations of Δ_F^2 would inform He II reionization models.

The contribution from $P_{Tp7\Delta}$ to Δ_F^2 is of comparable import to the contribution from P_{Tp7} in the four cases considered in Figure 11, despite $P_{Tp7\Delta}$ being smaller than P_{Tp7}. This occurs because $P_{Tp7\Delta}$ is enhanced relative to P_{Tp7} by a factor of 2ϵ in equation (4). This enhancement explains why the temperature fluctuations in the simulations produce a comparable change in Δ_F^2 to that in our toy temperature model, despite the toy model having a much larger P_T. If the He II ionizers were more abundant than assumed here (as would be the case if the faint end of the quasar luminosity function were steeper; Furlanetto & Oh 2008a), $P_{Tp7\Delta}$ could be significantly larger, increasing the impact of temperature fluctuations on P_F.

In conclusion, temperature fluctuations could have a significant effect on the 3D power spectrum in the forest and would be detectable in future 3D Lyα forest analyses such as with BOSS. Our simple analytic description for their impact is extremely successful.

5   INTENSITY FLUCTUATIONS

Several studies have investigated the impact of intensity (J) fluctuations on the Lyα forest (Zuo 1992a,b; Meiksin & White 2004; Croft 2004; McDonald et al. 2005;

Furlanetto 2009; Mesinger & Furlanetto 2009). Here we attempt to understand how intensity fluctuations could affect 3D correlations in the forest. Meiksin & White (2004) and Croft (2004) concluded that J fluctuations have a small effect at $10-100$ km s^{-1} separations in the Lyα forest correlation function, but found that they could change this statistic at the 10s of percent-level on larger scales. Interestingly, White et al. (2010) found that intensity fluctuations could have an order-unity impact on 3D correlations. A detection of intensity fluctuations would constrain the rarity of the sources of ionizing photons, and it would constrain the contribution of quasars versus that of galaxies to the metagalactic ionizing background.

Intensity fluctuations (equivalent to Γ_{-12} fluctuations) alter the 3D Lyα forest power spectrum on linear scales as

$$P_F(\boldsymbol{k}) \approx \tilde{P}_F(\boldsymbol{k}) + b^2 \left[\epsilon^{-2} P_J(k) - 2\,\epsilon^{-1}(1+g\mu^2)\,P_{\Delta J}(k) \right],$$
(6)

(c.f. eqn. 4) where $\tilde{P}_F(\boldsymbol{k})$ is the flux power-spectrum without J fluctuations. If we assume a Euclidean space in which all H I ionizing photons experience a single attenuation length λ and treat the quasars as continuously shining lightbulbs, then

$$P_J = \left(\frac{\arctan(\lambda k)}{\lambda k} \right)^2 \left(\frac{\langle L^2 \rangle}{\bar{n}\,\langle L \rangle^2} + b_q^2\,P_\Delta(k) \right),$$
(7)

(which is similar to the expression for P_J in Mesinger & Furlanetto 2009) and

$$P_{\Delta J} = \left(\frac{\arctan(\lambda k)}{\lambda k} \right) b_q\,P_\Delta(k).$$
(8)

Here, P_J, is the power spectrum of intensity fluctuations, $P_{\Delta J}$ is the cross correlation between intensity and density, b_q and $\bar{n}$ are respectively the luminosity-weighted bias and 3D number density of the sources, and $(\lambda k)^{-1}\arctan(\lambda k)$ is (up to a constant factor) the Fourier transform of $r^{-2}\exp[-r/\lambda]$.[4]

Finite quasar lifetimes alter P_J when the lifetime t_q is comparable to or shorter than λ/c, or 300 Myr for $\lambda = 100$ proper Mpc. The variance of J does not depend on t_q when normalizing to a single luminosity function, but finite lifetimes can reduce large-scale J correlations because J becomes uncorrelated in regions separated by distances greater than $> c\,t_q$. These effects can be included in equation (6) by substituting a more complicated window function for $(\lambda k)^{-1}\arctan(\lambda k)$. However, the primary effect is for P_J to become white at wavelengths greater than $c\,t_q$ rather than at $\sim\lambda$. Thus, detecting intensity fluctuations on 100 Mpc scales would place interesting constraints on

---

[4] A commonly used formula for the correlation function of intensity fluctuations, ξ_J, is

$$\xi_J(r) = \frac{1}{3\,N}\,\frac{\langle L^2 \rangle}{\langle L \rangle^2}\,\frac{\lambda}{r}\,I_J\!\left(\frac{r}{\lambda}\right),$$
(9)

with

$$I_J(u) = 2\int_0^\infty dv\,\frac{v}{\sinh v}\,\exp\left[-u\,\frac{1+e^{-v}}{1-e^{-v}}\right],$$
(10)

and $N = 4\pi\lambda^3\bar{n}/3$. Note that this formula for ξ_J (derived by fairly complicated means in Zuo 1992b) is just the convolution of $r^{-2}\exp[-r/\lambda]$ with itself (times a factor that depends on the luminosity function). Put another way, it is the Fourier transform of the Poissonian term in equation (7).
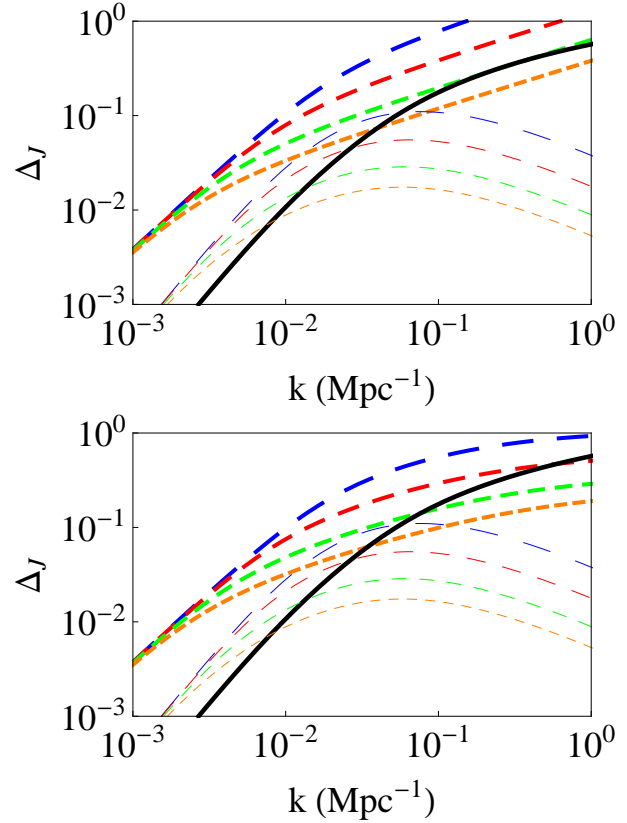

Figure 12. Top panel: Dimensionless power spectrum of intensity fluctuations to the 1/2 power. The thick dashed curves are the Poisson component, and the thin dashed are the clustered component. Both sets of curves assume $\lambda = 500, 300, 150$, and 70 Mpc (from bottom to top), corresponding roughly to the mean free path at $z = 2, 3, 4$, and 5. For reference, the thick black curve is $[k^3\,P_\Delta/2\pi^2]^{1/2}$ in linear theory at $z = 3$. The Poisson-component curves assume $\bar{n} = 10^{-4}$ Mpc^{-3} and $\langle L^2 \rangle/\langle L \rangle^2 \approx 30$, which set these curves' normalizations. The clustering curves assume $b_q = 3$ and $z = 3$. Bottom panel: Same as the top panel but where the power from the proximity region is smoothed out for the Poissonian curves as described in the text. Note that 10^{-2} Mpc^{-1} is approximately the smallest wavevector that can be estimated from the forest.

quasar lifetimes. In addition, light travel effects alter the isotropy of the J fluctuations because the emission will have travelled further in the line-of-sight direction. This would result in additional μ-dependent terms in equation (7).

The top panel in Figure 12 plots the Poisson and clustering components of $\Delta_J \equiv [k^3\,P_J/2\pi^2]$ (the first and second terms in eqn. 7) for infinite lifetimes. The thick dashed curves are the Poisson component for $\lambda = 500, 300, 150$, and 70 Mpc (in order of decreasing amplitude). For reference, these λ correspond roughly to its measured value at $z = 2, 3, 4$ and 5 (Faucher-Giguère et al. 2008; Prochaska et al. 2009). Our calculations assume that the quasar luminosity function has the form $\Phi(L) \sim ([L/L_*]^\alpha + [L/L_*]^\beta)^{-1}$ with a cutoff 3 decades above and below L_*, where $\alpha = 1.5$ and $\beta = 3.5$. These choices result in $\langle L^2 \rangle/\langle L \rangle^2 \approx 30$. Changing both the upper and lower cutoff by a factor of 10 and in opposite directions results in a factor of 3 change in $\langle L^2 \rangle/\langle L \rangle^2$. Furthermore, the curves in the top panel in Figure 12 use $\bar{n} = 10^{-4}$ Mpc^{-3}, representative of quasars at $z = 2 - 3$.

The Hopkins et al. (2007) quasar luminosity function yields $\bar{n} = \{1.2 \times 10^{-4}, \ 9 \times 10^{-5}, \ 5 \times 10^{-5}, \ 2 \times 10^{-5}\}$ Mpc^{-3} at $z = \{2.5, \ 3, \ 4, \ 5\}$.

For three of the four cases featured in the top panel in Figure 12, the power in the Poisson component is *always* larger than the power in the density field (the black solid curve). However, the normalization of the Poissonian component of Δ_J is highly uncertain. The Poisson curves in the top panel of Figure 12 are roughly a factor of 3 below the corresponding estimate in Furlanetto (2009) in part because Furlanetto (2009) used $\beta = 2.9$ for which $\langle L^2 \rangle / \langle L \rangle^2 \approx 100$ with our luminosity cutoffs. Most investigations of J fluctuations on the forest have used values for β that are more similar to the value used here (Meiksin & White 2004; Croft 2004; McDonald et al. 2005). However, Furlanetto (2009) argued that $\beta = 2.9$ provides a better fit to the Hopkins et al. (2007) luminosity function.

The thin dashed curves in the top panel in Figure 12 represent the contribution to Δ_J from source clustering at $z = 3$ for $b_q = 3$ and for the same λ as the corresponding thick curve. These curves fall below the Poisson component with the same λ. However, the clustering component of intensity fluctuations will likely be the dominant source of J fluctuations if galaxies are the source of ionizing photons (as several studies have argued might be the case at $z \gtrsim 4$; e.g. Faucher-Giguère et al. 2008). Because the clustered component also affects the flux field via $P_{\Delta J}$, this will enhance its effect beyond its contribution to P_J and also allow this contribution to be separated via its distinct angular dependence (Section 6). In addition, the power in the clustering component of J is always larger than that in the density — the standard source of fluctuations in the forest — at $k \lesssim \lambda^{-1}$ since $b_q > 1$. These scales become observable in the Lyα forest at $z \gtrsim 3$.

5.1   Effect of Intensity Fluctuations on P_F

The previous section showed that P_J can be comparable to P_Δ in the Lyα forest. If our simple analytic expression is correct (eqn. 6), this implies that J fluctuations significantly increase P_F beyond $\tilde{P}_F$. However, previous numerical studies of the impact of intensity fluctuations on $P_F^{\rm los}$ have considered models where the power in J was comparable to or larger than the power in Δ_b, and these studies found that these fluctuations had a small effect on $P_F^{\rm los}$ for $k > 0.1$ Mpc^{-1} (e.g., Croft 2004; McDonald et al. 2005). Here we try try to resolve this apparent discrepancy.

Figure 13 features numerical calculations of the impact of intensity fluctuations on Δ_F^2. The thin black dashed curve is the contribution to the total power from intensity fluctuations using equation (6) and the fiducial model for J fluctuations with $\lambda = 300$ Mpc. To generate the J field, we have convolved a random distribution of quasars which have the said luminosity function with the function $r^{-2} \exp[-r/\lambda]$. This ignores the clustering contribution, which Figure 12 suggests is smaller but non-negligible in this model. The solid red curve is Δ_F^2 without intensity fluctuations, and the dashed green is the fully numerical calculation of the effect of intensity fluctuations in this model. The blue dotted curve is the prediction of equation (6) – the addition of the dashed black and solid red curves. The analytic model does poorly at capturing the impact of intensity fluctuations
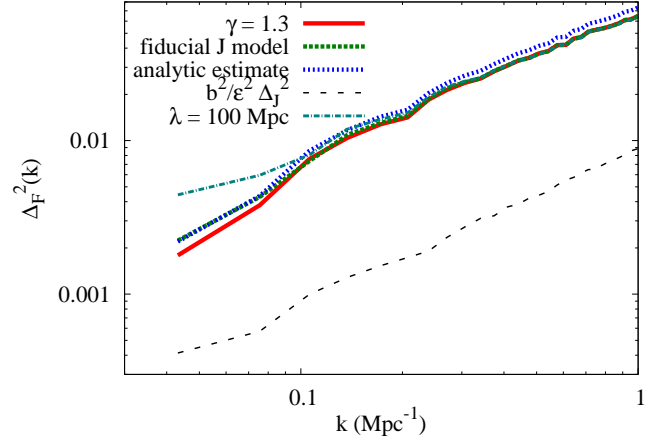

Figure 13. Impact of intensity fluctuations on Δ_F^2 at $z = 3$, calculated using the 190 Mpc simulation. The solid red curve represents this for a uniform intensity field, and the blue dotted represents this for a fluctuating field with $\lambda = 300$ Mpc, $\langle L^2 \rangle / \langle L \rangle^2 = 30$, and $\bar{n} = 10^{-4}$ Mpc^{-3}. The green dashed curves are the predictions by adding Δ_J^2 to $\tilde{\Delta}_F^2$ as specified by equation (6). The dashed black curve is $b^2/\epsilon^2 \Delta_J^2$ in this model, and the teal dot-dashed curve is the same as the green dashed but for a model with $\lambda = 100$ Mpc.

at $k > 0.1$ Mpc^{-1}, but does better at smaller wavevectors. The teal dot-dashed curve is the same as the green dashed but for a model with $\lambda = 100$ Mpc such that the intensity fluctuations are larger and thus have a larger impact on Δ_F^2.

The poor performance of the analytic model at $k > 0.1$ Mpc^{-1} owes to the diverging character of J in quasar proximity regions. Within the proximity region of a quasar (within the distance $r_p(L) \equiv [4\pi\langle L\rangle/L\,\bar{n}\,\lambda]^{-1/2}$), the effect on Δ_F^2 will be suppressed beyond the prediction in equation (6) by the exponential transformation from $\tau_{\rm Ly\alpha}$ to transmission. Because $\tau_{\rm Ly\alpha} \sim (1 + [r_p/r]^2)^{-1}$, the small-scale transmission power from proximity regions is damped exponentially with a kernel similar to that of a Gaussian with s.d. $\approx r_p^{-1}/\sqrt{2}$. The bottom panel in Figure 12 is the same as the top panel, but where for the Poisson term in P_J given by $k^{3/2} \arctan(\lambda k)/\lambda k$ has been forced to transition to a constant function of k with the transition occurring at $k = r_p(L)^{-1}/\sqrt{2}$. This operation is meant to approximate the convolution of $\arctan(\lambda k)/\lambda k$ with the Gaussian-like shape of the proximity region. The power in J is significantly affected by this operation at the largest k that are shown. The k where the proximity-region damping occurs are roughly $k \gtrsim r_p(\langle L^2\rangle^{1/2})^{-1}$, which correspond to $k \gtrsim 0.1$ Mpc^{-1} in our fiducial model. Smaller k correspond to where the analytic model provides a good description in Figure 13.

Density fluctuations become larger than those in J at $k > 0.3$ Mpc^{-1} in three of the Poissonian models in the bottom panel of Figure 12 (and the intensity power is also suppressed by an additional factor of ϵ^2 in Δ_F^2). Wavevectors with $k > 0.3$ Mpc^{-1} correspond roughly to those where $P_F^{\rm los}$ has been measured. As with temperature fluctuations, the impact of intensity fluctuations are further diluted by aliasing in $P_F^{\rm los}$ such that 3D fluctuations are better suited for detecting them. Thus, it is unlikely that the intensity fluctuations in three of these models would have produced a detectable imprint on $P_F^{\rm los}$. In fact, we have calculated the

impact of our fiducial J model on $P_F^{\rm los}$ in the $25/h$ Mpc box and, because of this small-scale damping, found no appreciable effect owing to these damping and aliasing effects.

At $z \gtrsim 4$, it is conceivable that intensity fluctuations contribute a substantial portion of the power even in $P_F^{\rm los}$ because both λ and $\bar{n}$ are smaller. Interestingly, McDonald et al. (2005) constrained the $z = 4$ mean flux from power spectrum measurements to be $10 - 20\%$ higher than the more direct measurement in Faucher-Giguère et al. (2008). Such a disparity could potentially occur if an unaccounted source of fluctuations were contributing to $P_F^{\rm los}$. Some of the intensity models considered in McDonald et al. (2005) [their Fig. 5] and more generally in models where $\langle L^2 \rangle / [\langle L \rangle^2 \, \lambda^2 \, \bar{n}] \gtrsim 10^2$ Mpc are able to produce a tens of percent change in the power at all scales.

There are several possibilities for how the impact of intensity fluctuations on P_F can be distinguished from the fluctuations in the temperature. Temperature fluctuations should peak in amplitude at $z = 2.5 - 3$ if He II reionization were ending around these redshifts. In contrast, intensity fluctuations are likely to have increased monotonically with redshift. In addition, the amplitude of P_J is set by the factor $\langle L^2 \rangle / [\langle L \rangle^2 \, \lambda^2 \, \bar{n}_{\rm 3D}]$, which can potentially be constrained by ancillary observations.

6   SEPARATING THE COMPONENTS OF P_F

The signal we are interested in has the form $P_F = P_0 + 2g\,\mu^2 P_1 + g^2\mu^4 P_2$ in linear theory, where the P_i are functions of only $k \equiv |\mathbf{k}|$ and are given by $P_0 = b^2\,P_\Delta + b^2\,\epsilon^{-2}\,[P_J + P_{Tp7}]$, $P_1 = 2\,b^2\,P_\Delta + 2\,b^2\,\epsilon^{-1}\,[P_{\Delta J} + P_{\Delta Tp7}]$, and $P_2 = b^2\,P_\Delta$. Thus, temperature and intensity fluctuations affect P_0 and, to the extent they correlate with density, P_1. (Light-travel effects can generate additional μ^{2n} terms that we do not consider.) Here we investigate the sensitivity of a survey to the terms in this angular decomposition. Detecting these angular components may prove easier in the Lyα forest than it has for galaxy surveys because the velocity bias g is likely to be larger in the Lyα forest than in galaxy surveys (for which $g = 1/b_g$, where b_g is the galaxy bias).

The Fisher matrix for the parameters P_i is

$$\mathbf{F}_{\rm ij} = \sum_{\rm k-shell} \frac{1}{{\rm var}[P_F(\mathbf{k})]} \, \frac{dP_F(\mathbf{k})}{dP_i} \frac{dP_F(\mathbf{k})}{dP_j}, \qquad (11)$$

where the sum is over $\mathcal{N}_k$ independent elements in a shell in k-space centered at distance $|\mathbf{k}|$ from the origin. In addition, ${\rm var}[P_F(\mathbf{k})]$ is the variance on an estimate of P_F in a pixel centered on $\mathbf{k}$.

Let us first approximate ${\rm var}[P_F(\mathbf{k})]$ as isotropic, which is the relevant limit for BOSS and, more generally, for all surveys with less than 100 Lyα forest spectra per degree (White et al. 2010; McQuinn & White 2011). In this limit, the error on a measurement of P_i is

$$\boldsymbol{\sigma}(k) \equiv [\mathbf{F}^{-1}]^{1/2}{}_{ii} = \frac{{\rm var}[P_F(k)]^{1/2}}{\sqrt{\mathcal{N}_k}} \, (1.5, \ 4.0\,g^{-1}, \ 10.7\,g^{-2}). \tag{12}$$

Also informative is the cosmic variance limit in which ${\rm var}[P_F(\mathbf{k})] = 2\,b^4\,P_\Delta(k)^2\,(1 + g\mu^2)^4$, and for $g = 1$ results in

$$\boldsymbol{\sigma}(k) = \sqrt{\frac{2}{\mathcal{N}_k}}\,b^2\,P_\Delta(k)\,(2.1, \ 20.4, 28.2). \tag{13}$$

In both limits, a survey detects P_0 at the highest significance. P_1 reveals how the temperature and photoionization fluctuations correlate with those of density. Because BOSS can constrain P_F in bins of $\Delta k \sim k$ at $z \sim 2.5$ at the 1% level, it should also be able to place 10%-level constraints on P_1.

7   CONCLUSIONS

Significant temperature fluctuations with $\Delta T/T \approx 1$ were likely imprinted in the high-redshift IGM by reionization processes, and they would have lasted for roughly a Hubble time thereafter. Temperature fluctuations would have been imprinted at $z \sim 3$ if He II reionization were ending near this redshift and, thereby, affected the majority of Lyα forest spectra. In addition, if hydrogen reionization ended at $z \approx 6$, remnant temperature fluctuations could still be observable in the forest from redshifts as low as $z = 4$ (e.g., Cen et al. 2009). This paper investigated the detectability of these fluctuations.

Previous studies have shown that the $z = 2 - 4$ IGM cannot have been half filled with ~ 10 Mpc patches of temperature 20 kiloK and the rest at 10 kiloK (Theuns et al. 2002; Lidz et al. 2010). However, we showed that half with $T_0 = 25$ kiloK and half with $T_0 = 15$ kiloK is consistent with recent Lyα forest analyzes. Such a temperature distribution is also close to what is found near the end of He II reionization in the radiative transfer simulations of McQuinn et al. (2009). If fact, we showed that the temperature history in the fiducial simulation of He II reionization in McQuinn et al. (2009) is grossly consistent with previous Lyα forest measurements, although the observations tentatively favor less evolution in the mean temperature. The temperature fluctuations in this simulation do not alter the small-scale Lyα forest power spectrum (Section 4.1), the PDF of the normalized flux (Section 4.2), the large-scale line-of-sight power spectrum (Section 4.3), the wavelet PDF (Appendix A), and the three-point statistic proposed in Zaldarriaga et al. 2001 (Appendix A) in a manner that is distinguishable from a power-law $T - \Delta_b$ relation. Thus, the temperature fluctuations produced during a $z \sim 3$ He II reionization by quasars would probably have evaded previous searches and also likely would evade future searches using these standard statistics.

Interestingly, we find that realistic models for large-scale temperature fluctuations could have a significant effect on the 3D Lyα forest power spectrum. This statistic can be measured by cross-correlating multiple quasar sightlines. In the line-of-sight power spectrum, the aliasing of small-scale 3D density power to larger scale line-of-sight modes dramatically suppresses the prominence of temperature fluctuations for physically motivated models. However, we found that physically motivated temperature models could impart an order unity increase in the 3D power at $k \sim 0.1$ Mpc^{-1}. We showed that the impact of temperature fluctuations on the 3D power spectrum could be understood with a simple analytic model.

Intensity fluctuations could also alter the large-scale correlations in the Lyα forest. These too would have been hidden in the line-of-sight power spectrum by aliasing effects. At sufficiently large scales, intensity fluctuations will

be the dominant source of fluctuations in the forest, and the fluctuations will become more prominent with increasing redshift. The impact of intensity fluctuations on P_F is likely to be distinguishable spectrally from the impact of temperature inhomogeneities.

BOSS is forecasted to measure the 3D flux power spectrum P_F with percent-level accuracy at $z \approx 2.5$ in a k-space shell with $\Delta k \sim k$. Such a measurement would constrain the effects discussed here, and we anticipate that these extra sources of fluctuations can be distinguished from other uncertainties in P_F (such as in the cosmology) when their impact is larger than $\sim 10\%$. In addition, BOSS is capable of placing interesting constraints on this statistic to redshifts as high as $z \approx 3$ and BigBOSS to $z \approx 4$. Deeper surveys on an $8-10$ m class telescope can push this measurement to even higher redshifts (McQuinn & White 2011). Furthermore, P_F can be separated into different angular components with BOSS and future quasar surveys, which will facilitate the separation of the density, intensity, and temperature contributions. The cross correlation of the Lyα forest with another tracer of large-scale structure (such as a high-z galaxy survey) could also enable this separation (Guha Sarkar et al. 2011; McQuinn & White 2011).

The impact of temperature and intensity fluctuations will complicate attempts to constrain cosmic distances using the BAO features in the 3D Lyα forest. Because there is not one unique template for the spectrum of T and J fluctuations, marginalizing over their potential impact would likely require a fairly general parameterization for the continuum on which the BAO sits. Such a marginalization procedure would reduce the sensitivity to cosmological parameters. Temperature and intensity fluctuations may also impart (via their correlation with density) a scale dependence to the BAO amplitude.

Cen et al. (2009) found that temperature fluctuations from models of H I reionization had a larger effect on the line-of-sight Lyα forest power spectrum than we have found in our temperature models. They examined $P_F^{\rm los}$ at $z=4$ and $z=5$, using simulations of hydrogen reionization. They found that temperature fluctuations resulted in an increase in $P_F^{\rm los}$ by $5-10\%$ at $k \sim 10^{-2}$ s km^{-1} and $20-30\%$ at $k \sim 10^{-3}$ s km^{-1} – the latter being roughly an order of magnitude larger than what our temperature models produce at $z=3$. The larger effect found in Cen et al. (2009) likely owes to two reasons. First, if the hydrogen were reionized by numerous dwarf galaxies as is assumed in the Cen et al. (2009) simulations, there would have been a stronger anti-correlation after this process completed between T and the large-scale density at relevant scales than in our He II reionization simulations. The effect of temperature fluctuations on $P_F^{\rm los}$ could be significantly enhanced by such an anti-correlation, as can be noted from equation (4). Second, the density power decreases with increasing redshift, which results in the temperature fluctuations (which tend to have $\Delta T/T \sim 1$ because of the photoionization physics) becoming relatively larger. The impact of temperature fluctuations in the Cen et al. (2009) models should be even more dramatic on the 3D Lyα forest power spectrum.

REFERENCES

Abel T., Haehnelt M. G., 1999, ApJL, 520, L13
Agafonova I. I., Levshakov S. A., Reimers D., Fechner C., Tytler D., Simcoe R. A., Songaila A., 2007, *A.&A*, 461, 893
Becker G. D., Bolton J. S., Haehnelt M. G., Sargent W. L. W., 2011, MNRAS, 410, 1096
Bolton J. S., Becker G. D., Wyithe J. S. B., Haehnelt M. G., Sargent W. L. W., 2010, MNRAS, 406, 612
Bolton J. S., Viel M., Kim T., Haehnelt M. G., Carswell R. F., 2008, MNRAS, 386, 1131
Cen R., McDonald P., Trac H., Loeb A., 2009, ApJL, 706, L164
Croft R. A. C., 2004, ApJ, 610, 642
Croft R. A. C., Weinberg D. H., Bolte M., Burles S., Hernquist L., Katz N., Kirkman D., Tytler D., 2002, ApJ, 581, 20
Davé R., Hernquist L., Katz N., Weinberg D. H., 1999, ApJ, 511, 521
Davidsen A. F., Kriss G. A., Zheng W., 1996, Nature, 380, 47
Dixon K. L., Furlanetto S. R., 2009, ApJ, 706, 970
Fang T., White M., 2004, ApJL, 606, L9
Faucher-Giguère C., Lidz A., Hernquist L., Zaldarriaga M., 2008, ApJL, 682, L9
Faucher-Giguère C., Prochaska J. X., Lidz A., Hernquist L., Zaldarriaga M., 2008, ApJ, 681, 831
Furlanetto S. R., 2009, ApJ, 700, 1666
Furlanetto S. R., Dixon K. L., 2010, ApJ, 714, 355
Furlanetto S. R., Oh S. P., 2008a, ApJ, 682, 14
Furlanetto S. R., Oh S. P., 2008b, ApJ, 681, 1
Gnedin N. Y., Hui L., 1998, MNRAS, 296, 44
Guha Sarkar T., Bharadwaj S., Choudhury T. R., Datta K. K., 2011, MNRAS, 410, 1130
Hernquist L., Katz N., Weinberg D. H., Miralda-Escudé J., 1996, ApJL, 457, L51+
Hopkins P. F., Richards G. T., Hernquist L., 2007, ApJ, 654, 731
Hui L., Gnedin N. Y., 1997, MNRAS, 292, 27
Hui L., Haiman Z., 2003, ApJ, 596, 9
Kaiser N., 1987, MNRAS, 227, 1
Katz N., Weinberg D. H., Hernquist L., Miralda-Escude J., 1996, ApJL, 457, L57+
Kim T., Bolton J. S., Viel M., Haehnelt M. G., Carswell R. F., 2007, MNRAS, 382, 1657
Komatsu E., et al., 2011, ApJS, 192, 18
Lai K., Lidz A., Hernquist L., Zaldarriaga M., 2006, ApJ, 644, 61
Lee K., 2011, ArXiv e-prints
Lee K., Spergel D. N., 2010, arxiv:1007.3734
Lidz A., Faucher-Giguère C., Dall'Aglio A., McQuinn M., Fechner C., Zaldarriaga M., Hernquist L., Dutta S., 2010, ApJ, 718, 199
McDonald P., 2003, ApJ, 585, 34
McDonald P., et al., 2005, ApJ, 635, 761

McDonald P., Miralda-Escudé J., Rauch M., Sargent W. L. W., Barlow T. A., Cen R., 2001, ApJ, 562, 52

McDonald P., Miralda-Escudé J., Rauch M., Sargent W. L. W., Barlow T. A., Cen R., Ostriker J. P., 2000, ApJ, 543, 1

McDonald P., Seljak U., Cen R., Bode P., Ostriker J. P., 2005, MNRAS, 360, 1471

McQuinn M., 2009, ApJL, 704, L89

McQuinn M., Lidz A., Zaldarriaga M., Hernquist L., Hopkins P. F., Dutta S., Faucher-Giguère C., 2009, ApJ, 694, 842

McQuinn M., White M., 2011, ArXiv e-prints

Meiksin A., 2000, MNRAS, 314, 566

Meiksin A., White M., 2004, MNRAS, 350, 1107

Mesinger A., Furlanetto S., 2009, MNRAS, 400, 1461

Miralda-Escudé J., Haehnelt M., Rees M. J., 2000, ApJ, 530, 1

Miralda-Escudé J., Cen R., Ostriker J. P., Rauch M., 1996, ApJ, 471, 582

Miralda-Escudé J., Rees M. J., 1994, MNRAS, 266, 343

Peacock J. A., Dodds S. J., 1996, MNRAS, 280, L19

Peeples M. S., Weinberg D. H., Davé R., Fardal M. A., Katz N., 2010, MNRAS, 404, 1281

Prochaska J. X., Worseck G., O'Meara J. M., 2009, ApJL, 705, L113

Ricotti M., Gnedin N. Y., Shull J. M., 2000, ApJ, 534, 41

Schaye J., Theuns T., Rauch M., Efstathiou G., Sargent W. L. W., 2000, MNRAS, 318, 817

Shull M., France K., Danforth C., Smith B., Tumlinson J., 2010, ArXiv e-prints

Slosar A., Ho S., White M., Louis T., 2009, Journal of Cosmology and Astro-Particle Physics, 10, 19

Springel V., 2005, MNRAS, 364, 1105

Theuns T., Schaye J., Haehnelt M. G., 2000, MNRAS, 315, 600

Theuns T., Schaye J., Zaroubi S., Kim T., Tzanavaris P., Carswell B., 2002, ApJL, 567, L103

Theuns T., Zaroubi S., 2000, MNRAS, 317, 989

Theuns T., Zaroubi S., Kim T.-S., Tzanavaris P., Carswell R. F., 2002, MNRAS, 332, 367

Trac H., Cen R., Loeb A., 2008, ApJL, 689, L81

Viel M., Bolton J. S., Haehnelt M. G., 2009, MNRAS, pp L290+

White M., Pope A., Carlson J., Heitmann K., Habib S., Fasel P., Daniel D., Lukic Z., 2010, ApJ, 713, 383

Zaldarriaga M., 2002, ApJ, 564, 153

Zaldarriaga M., Hui L., Tegmark M., 2001, ApJ, 557, 519

Zaldarriaga M., Seljak U., Hui L., 2001, ApJ, 551, 48

Zuo L., 1992a, MNRAS, 258, 36

Zuo L., 1992b, MNRAS, 258, 45

APPENDIX A: OTHER LINE-OF-SIGHT STATISTICS

A1 Wavelets

Several studies have suggested using wavelet functions to search for temperature fluctuations in the Lyα forest (Meiksin 2000; Theuns et al. 2002; Zaldarriaga 2002). This method uses the wavelet property that they are localized in configuration in addition to Fourier space. The idea is
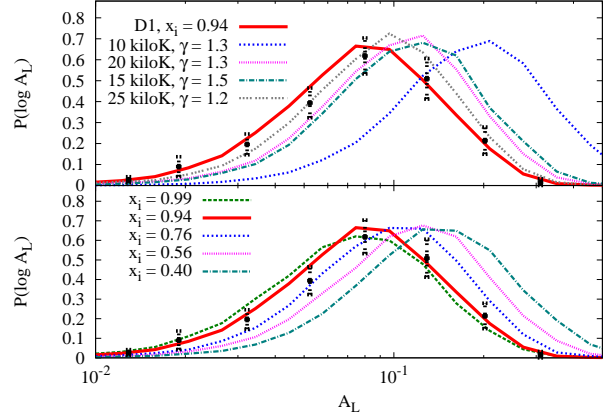
Figure A1. PDF of the wavelet coefficients A_L with $L = 500$ km s^{-1} for several temperature models. The points with errorbars are from the $z = 3$ measurement of Lidz et al. (2010) and the solid red curves represent the $z = 3$ snapshot in the simulation.
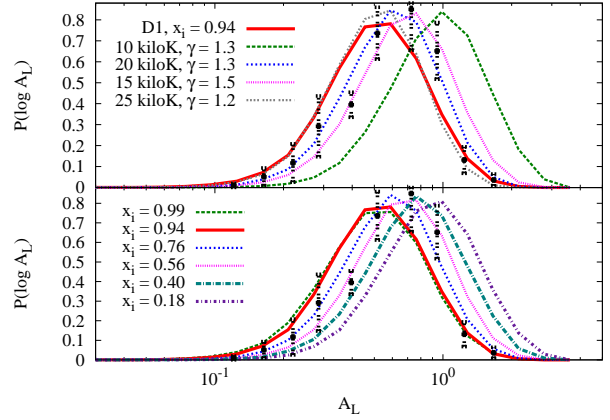

Figure A2. Same as Figure A1 but for $z = 4.2$. The teal curve in the bottom panel represents the $z = 4$ snapshot in the simulation.

to convolve the Lyα forest transmission field with a wavelet that is sensitive to the amount of small-scale power to search for spatial variations in the power and, thus, temperature fluctuations.

We compare the wavelet predictions of different temperature models with the recent measurement by Lidz et al. (2010). This study applied this technique to 40 high resolution, high S/N Lyα forest spectra spanning $2 \lesssim z \lesssim 4.5$. The wavelet filter that Lidz et al. (2010) used is

$$\Psi(x) = C \exp\left(i k_0 x\right) \exp\left[-\frac{x^2}{2\,s_n^2}\right]. \qquad (A1)$$

Lidz et al. (2010) chose C such that $\Sigma_{i=1}^N \Delta x\,\Psi(x)^2/N = 1$ for $\Delta x = 4.4$ km s^{-1}. Lidz et al. (2010) found $s_n = 69.7$ km s^{-1} and $k_0\,s_n = 6$ to be a good compromise between maximizing sensitivity to temperature while minimizing the impact of instrumental noise. Conveniently, the Fourier transform of $\Psi(x)$, which we denote as $\tilde{\Psi}(k)$, is a Gaussian centered around $k = k_0$ with standard deviation s_n^{-1}. The full width half maximum of $\tilde{\Psi}(k)$ spans

$0.06 < k < 0.1 \text{ s km}^{-1}$, and $\tilde{\Psi}(k)$ is plotted in the top panels in Figures 5 and 6 (thin curves, arbitrarily normalized). The wavelet filter that was used in other wavelet studies of the forest is qualitatively similar to the Lidz et al. (2010) filter, and we expect our conclusions are robust to the exact filter choice (such as the curvature statistic of Becker et al. 2011).

Lidz et al. (2010) primarily analyzed the PDF of

$$A_L(x) = \frac{1}{2L} \int_{-L}^{L} dx \, |\Psi(x) \circ \delta_F(x)|^2 , \qquad \text{(A2)}$$

where "$\circ$" denotes a convolution, and the integral averages the convolved signal over $L = 500 \text{ km s}^{-1}$ in order to reduce the noise. Thus, their A_L was the average of the wavelet power in a ≈ 10 Mpc region. The mean of this PDF is sensitive to the average temperature (because it is a measure of the average power within the wavelet bandpass), whereas the width is a measure of the spatial variance in the temperature. However, cosmic variance in the forest is the primary determinant of the width of this PDF, and temperature fluctuations would manifest as an excess in the width over what is expected from simple models for the IGM thermal state.

Figures A1 and A2 plot the predictions for the wavelet PDF at $z = 3$ and $z = 4.2$ using different temperature models. These curves were calculated from the same simulation skewers as the P_F^{los} curves in Figures 5 and 6. The points with error bars are the measured values from Lidz et al. (2010). The top panel in both figures explore toy power-law $T - \Delta_b$ models. (See Lidz et al. (2010) for a more extensive comparison of such models.)

The wavelet PDF of the $\gamma = 1.3$, $T_0 = 10$ kiloK model is quite discrepant with that of the $\gamma = 1.3$, 20 kiloK model (Fig. A1). The data favors the latter of these two models, and would also be inconsistent with a 50% mix of both temperatures (which would be the average of these two curves). Section 2 suggested that a more realistic toy fluctuating-temperature model is half the volume with $T_0 = 15$ kiloK and $\gamma = 1.5$ and the other half with $T_0 = 25$ kiloK and $\gamma = 1.2$. Unfortunately, the top panel illustrates that $T_0 = 15$ kiloK and $\gamma = 1.5$ produces a very similar wavelet PDF to the $T_0 = 25$ kiloK and $\gamma = 1.2$ case. Thus, as we found for P_F^{los} in Section 4.1, a 50% mix of these two models would be difficult to distinguish from a single T_0 and γ model.

The red solid curves in Figures A1 and A2 represent the simulation result near the end of He II reionization. These curves have a very similar width to the other curves in their respective panel despite the fact that these curves include dispersion in the temperature. The bottom panels show the wavelet PDF at different times during the simulation. Interestingly, none of these PDFs are noticeably broader than the power-law $T - \Delta_b$ case. Over the course of He II reionization in the simulation, the mean of the PDF shifts to smaller values owing to the heating of the simulated IGM. The teal and red curves represent the $z = 3$ and $z = 4$ outputs in the simulation. The mean of the PDF in the simulation appears to evolve slightly more between these redshifts than the data, consistent with what we found in Section 4.1.

In conclusion, measurements of the wavelet PDF constrain the mean temperature and place limits on temperature fluctuations at the level of $\Delta T/T \approx 1$ for slightly overdense gas. However, temperature fluctuations at the smaller level found in the simulations of McQuinn et al. 2009 do not
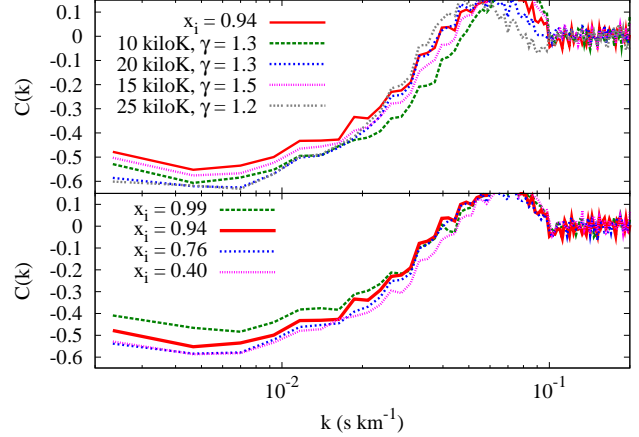

Figure A3. Three-point statistic outlined in Section A2, with $k_1 = 0.1$ and $k_2 = 0.2 \text{ s km}^{-1}$. The top panel shows this statistic for different power-law $T - \Delta_b$ models and for the temperature in the simulation snapshot with $x_{\text{HeIII}} = 0.94$. The bottom panel shows this statistic using the temperature from several snapshots of the He II reionization simulation.

significantly effect the width of the wavelet PDF and would be extremely difficult to detect with this statistic.

A2   Small-Scale Power – Large-Scale Flux Correlation

Zaldarriaga et al. (2001) and Fang & White (2004) discussed a particular three-point statistic that they argued provides an excellent test of the paradigm that gravitational instability shapes the transmission fluctuations in the Lyα forest. They advocated the statistic

$$C(k) \equiv \frac{P_{h\,\delta_F}(k)}{[P_h(k) \, P_{\delta_F}(k)]^{1/2}}, \qquad \text{(A3)}$$

where $P_{\delta_F}(k)$ is the power-spectrum of δ_F, $P_h(k)$ is this of h, and $P_{h\delta_F}(k)$ is the cross power between h and δ_F. Here, $h(x) \equiv \delta_H(x)^2$ and $\tilde{\delta}_H \equiv \tilde{\delta}_F(k) W_{k_1,k_2}(k)$, where $W_{k_1,k_2}(k)$ is a band-pass filter that transmits at $k_1 < k < k_2$ and tildes distinguish the Fourier dual. Thus, h is the square of the band pass-filtered flux field, making it a measure of the bandpass power. This statistic is normalized such that a perfect correlation between h with δ_F yields $C = 1$. Fang & White (2004) showed that this statistic could place strong constraints on the level of temperature fluctuations.

As in Zaldarriaga et al. (2001) and Fang & White (2004), we take $W_{k_1,k_2}(k)$ to be unity for $k_1 < k < k_2$ and zero otherwise. The statistic $C(k)$ is a measure of the correlation between δ_F and the small-scale power in the high pass-filtered Lyα transmission field. If gravity dominates the fluctuations in the forest, there will be more structure in a large-scale overdense (opaque) region, driving $C(k)$ negative. Predictions for $C(k)$ are shown in the top panel of Figure A3 for different power-law $T - \Delta_b$ models. The curves are calculated from the 1000, $25/h$ Mpc random skewers drawn from the $z = 3$ snapshot of the hydrodynamic simulation and with $k_1 = 0.1$ and $k_2 = 0.2 \text{ s km}^{-1}$. These curves all have $-0.6 < C < -0.5$ at $k \lesssim 0.01 \text{ km s}^{-1}$, and the curves with the largest γ have slightly smaller $|C|$. This trend re-

sults because, the larger the deviation from an isothermal relation, the more decorrelated a large-scale density mode is from the small-scale density power (Zaldarriaga et al. 2001).

Temperature fluctuations from reionization could also decorrelate the small-scale density power from the large-scale flux. However, temperature fluctuations could also enhance the negative correlation because a large-scale hot region has increased transmission and also less small-scale power. We find that the former effect is most important in our reionization simulations: These temperature fluctuations decrease $|C|$, but not significantly. The red solid curve in the top panel of Figure A3 uses the temperature fluctuations from the $x_{\text{HeIII}} = 0.94$ snapshot, and we find that $|C|$ is slightly smaller for this case compared to the power-law $T - \Delta_b$ models. The bottom panel in Figure A3 plots C using the temperature field from different snapshots of the He II reionization simulation.

Fang & White (2004) showed that adding a lognormal dispersion at the Jeans scale around the mean $T - \Delta_b$ relation with standard deviation 0.2 results in $|C|$ becoming significantly smaller. They used this result to constrain the standard deviation in this relation to be < 0.2 from a single quasar sightline. The temperature fluctuations in our He II reionization simulations have a standard deviation of $\sigma_T \approx 0.1$ (Fig. 2), but the simulations' temperature fluctuations are correlated over 10s of Mpc: In a large-scale hot or cold region, the dispersion in $T - \Delta_b$ is much smaller (Fig. 4). Likely because of these large-scale correlations, we find a significantly smaller suppression than in Fang & White (2004). Fang & White (2004) found the most dramatic effect for a higher pass filter than used in this section, in particular with $k_1 = 0.2$ and $k_2 = 0.3$ s km^{-1}. We find that if we use this filter choice, $|C|$ is reduced by a larger factor than for our fiducial filter (to a value as low as -0.3) but never to zero. However, even the choice $k_1 = 0.1$ and $k_2 = 0.2$ s km^{-1} is pushing the limit on what can be applied to even the highest quality Lyα forest data (Lidz et al. 2010).

APPENDIX B: PECULIAR VELOCITIES

This Appendix quantifies the impact of peculiar velocities on large-scale flux correlations. Peculiar velocities have two effects: (1) The large-scale peculiar velocity field results in a redshift-space compression so that more systems appear in regions with converging flows. (2) The nonlinear peculiar velocity compresses or dilates Jeans-scale dense regions in absorption space (and dilates Jeans-scale voids). On large scales, the latter effect enters by altering the bias of the forest. The former effect produces the redshift-space anisotropy of this signal. It affects $\tau_{\text{Ly}\alpha}$ via the factor $(H\,a + dv/dx)^{-1}$, where v and x are the peculiar velocity and comoving distance along the line of sight. In Fourier space this factor is simpler and approximately equal to $1 + \Omega_m(z)^{0.6}\mu^2\delta$, where $\mu = \hat{k} \cdot \hat{n}$ (Kaiser 1987). Thus, on linear scales the redshift-space power spectrum of δ_F is likely to have the form

$$P_F \approx b^2 \left[G^2\,P_\Delta + 2\,G\,\epsilon^{-1}\,P_{\Delta X} + \epsilon^{-2}\,P_X \right], \qquad \text{(B1)}$$

where $G = (1 + g\mu^2)$, g is the large-scale bias of velocity fluctuations, and X is a placeholder for T or $-J$ fluctuations. The average of G^2 over solid angle is 28/15. In linear theory, $g \approx \Omega_m(z)^{0.6}\,\epsilon^{-1}$. However, g will depart from the
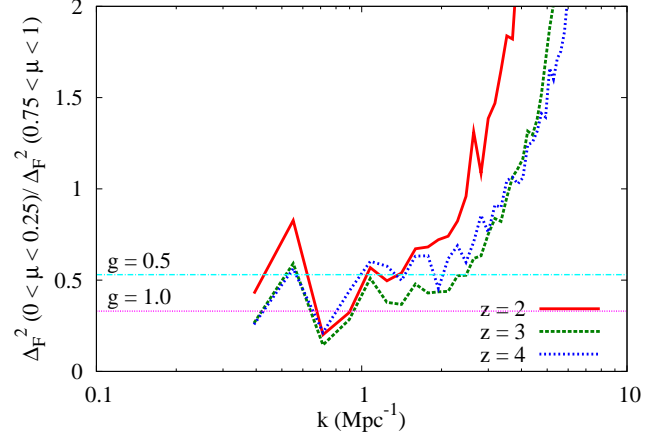

Figure B1. Ratio of the flux power spectrum for modes with $0 < \mu < 0.25$ to those with $0.75 < \mu < 1.0$. The curves are measured from the $25/h$ Mpc simulation at $z = 2, 3$ and 4, assuming $\gamma = 1.3$. The increase in these curves at small-scales owes to thermal broadening. The approximate plateau in the ratio provides a measure for g. The horizontal lines are the expected large-scale anisotropy for $g = 0.5$ and $g = 1.0$. A larger box size would be required for a more precise determination.

linear theory prediction in part because the absorption saturates in regions. In the limit that all the absorption is from saturated lines with bias b, $g = 1/b$. Interestingly, McDonald (2003) measured $g = 1.5$ at $z = 2$, larger than the linear theory prediction of $g \approx 0.5$. Slosar et al. (2009) found a value closer to unity from large box, low resolution simulations. We have also measured g from our $25/h$ Mpc, 2×512^3 hydrodynamic simulation and find values that are consistent with $g \approx 0.5 - 1$ (Fig. B1), although a larger box size is needed for a more precise determination.

APPENDIX C: A SECOND DERIVATION OF EFFECT OF INTENSITY FLUCTUATIONS ON P_F

This section develops a more sophisticated understanding for how Δ_F^2 is altered by large-scale temperature fluctuations. Let us assume $\xi_{Tp7}(r, \Delta_b)$ does not depend on Δ_b, where $\xi_{Tp7}(r, \Delta_b)$ is defined as the correlation function of $T_\Delta^{-0.7}/\langle T_\Delta^{-0.7}\rangle - 1$ and T_Δ is the mean temperature at a given Δ_b. This differs somewhat from our previous definition of the δ_{Tp7} field as the fluctuation field, but the distinction makes little difference in practice.

We define τ_0 as the Gunn-Peterson optical depth at $\Delta_b = 1$, and the value of τ_0 is set by the mean flux normalization. We also define $X \equiv \Delta^{2-.7\gamma}$ and the normalized flux as $F \equiv \exp[-\tau_0 X(1+\delta_T)]$. Finally, we neglect peculiar velocities, and we assume that the temperature fluctuations are uncorrelated with those in density and that they are Gaussian. While we found in Section 4.3.2 that the correlations with density are important and it is likely that the temperature fluctuations are not Gaussian, the results of this model are illustrative and generalize beyond these assumptions.

With these assumptions and definitions, the correlation between the normalized flux in a region with density Δ_1 and

a region separated by a distance r with Δ_2 is

$$
\begin{aligned}
\langle F_1 F_2 \rangle_T &= \int d\delta_{T_1} d\delta_{T_2} \; e^{-\tau_0 \left(X_1 (1+\delta_{T_1}) + X_2 (1+\delta_{T_2}) \right)} \\
&\quad \times \frac{e^{-\frac{1}{2}(\delta_{T_1} \, \delta_{T_2}) \mathbf{C}^{-1} (\delta_{T_1} \, \delta_{T_2})^T}}{\sqrt{(2\pi)^2 \det \mathbf{C}}}, \qquad (C1) \\
&= e^{-\tau_0 (X_1 + X_2)} \times \exp[\frac{\tau_0^2 \sigma_{Tp7}^2}{2} (X_1^2 + X_2^2)] \\
&\quad \times \exp\left[\tau_0^2 X_1 X_2 \, \xi_{Tp7}(r) \right], \qquad (C2) \\
&\approx \tilde{F}_1 \tilde{F}_2 \left(1 + \tau_0^2 X_1 X_2 \, \xi_{Tp7}(r) \right), \qquad (C3)
\end{aligned}
$$

where $\tilde{F} \equiv \exp[-\tau_0 X]$, $\mathbf{C} \equiv (1, \; \xi_{Tp7}/\sigma_{Tp7}^2; \; \xi_{Tp7}/\sigma_{Tp7}^2, \; 1)$, and $\langle ... \rangle_Y$ represents an ensemble average with respect to Y. To go from equation (C2) to equation (C3), we used that $\xi_{Tp7}(r) \ll 1$ to expand the exponential. Furthermore, we set the second exponential term in equation (C2) to unity. Since regions that dominate the flux correlation function have $\tau_0 X \sim 1$, the error from dropping this term is of order $\sigma_{Tp7}^2 \ll 1$. While this is comparable to the temperature term that we kept, it is less interesting because it does not depend on $\xi_{Tp7}(r)$. In addition, most of its effect is re-absorbed in the renormalization to a single mean flux.

To calculate the flux correlation function, we average $\langle F_1 F_2 \rangle_T$ over Δ_1 and Δ_2, which yields

$$
\xi_F \equiv \langle F_1 F_2 \rangle_{T\Delta} \approx \xi_{\tilde{F}(r)} + K^2 \xi_T(r) + \tau_0^2 \xi_{\tilde{F}}(r) \, \xi_T(r), \quad (C4)
$$

where $\xi_{\tilde{F}}(r)$ is the unperturbed flux correlation function and

$$
\begin{aligned}
K &= \tau_0 \langle F_1 X_1 \rangle_{\Delta_1}, \qquad (C5) \\
&= \tau_0 \int d\Delta \, \Delta^{2-.7\gamma} \exp[-\tau_0 \Delta^{2-.7\gamma}] \, p(\Delta). \qquad (C6)
\end{aligned}
$$

The function $p(\Delta_b)$ is the volume-weighted density probability distribution. We have dropped terms in equation (C4) that involve additional $\xi(r)$ factors as well as the connected moments that are not incorporated in $K^2 \xi_T(r)$.

We are interested in the impact of temperature fluctuations on $\gtrsim 10$ Mpc correlations. At these scales, it is justified to drop the last term in equation (C4). With these simplifications, the power spectrum of fluctuations in the normalized flux is given by

$$
P_F(k) \approx P_{\tilde{F}}(k) + \frac{K^2}{\bar{F}^2} P_T(k). \qquad (C7)
$$

Thus, the correction proportional to $\xi_T(r)$ has bias $K/\bar{F}$ in this model. We calculate $K^2/\bar{F}^2 = 0.18$ at $z = 4$ and 0.04 at $z = 3$, assuming $T_0 = 2 \times 10^4$ K, $\gamma = 1.3$, and $\Gamma_{\mathrm{HI}} = 10^{-12}$ s^{-1}, using the Miralda-Escudé et al. (2000) fitting function for $p(\Delta)$. It turns out that $K^2/\bar{F}^2$ is almost identical numerically to the corresponding factor that appears in equation (4), b^2/ϵ^2.